The Rare decay of $\Lambda_b \to \Lambda^0 \mu^+ \mu^-$ with the LHCb detector at CERN

MPhil Thesis

Daniel Elsby

The University of Birmingham
School of Physics and Astronomy

03/10/2012

Abstract:

The LHCb detector, one of the main particle physics detectors at the Large Hadron Collider (LHC) is purpose built for the study of interesting and rare particle physics events. One such rare event with an expected branching ratio of $\approx 10^{-6}$ is the decay of $\Lambda_b \to \Lambda^0 \mu^+ \mu^-$. This decay is interesting since it offers an opportunity to test our current understanding of particle physics and search for signs of new physics. In this thesis the background theory to the current model of particle physics (the Standard Model) and the main operational properties of the LHCb detector are summarized. The feasibility of observing this decay with LHCb is investigated and an estimated yield is calculated. A cut based selection is developed and optimized in order to select events according to this decay from the 2010 data set of approximately $1 fb^{-1}$ at a centre of mass energy of 7TeV. A clear indication of the decay is seen in the data with approximately 100 signal events and a significance of 4.8σ. The calculations of all required efficiencies are tabulated and are used to calculate a relative branching ratio to the resonant decay of $\Lambda_b \to \Lambda^0 J/\psi$, where $J/\psi \to \mu^+ \mu^-$, of $\mathcal{R} = 1.89 \times 10^{-3}$.

Contents

Chapter 1

Introduction

1.1 The Standard Model of Particle Physics

The fundamental interactions and processes in nature are governed by the Electromagnetic, Weak and Strong Forces and Gravity. Gravity is such a weak force that it is completely negligible at this scale. The Electromagnetic, Weak and Strong forces are described theoretically by the Standard Model of Particle Physics (SM). The SM is at the same time the most successful and well tested theory in the history of science. Despite this, it remains incomplete with many unanswered questions. The SM is a relativistic quantum field theory consisting of a fundamental set of particles from which everything is composed and contains all fundamental interactions in nature. Figure 1.1 [1] shows the 6 leptons, 6 quarks, 4 types of gauge boson and a scalar boson that make up the SM. The
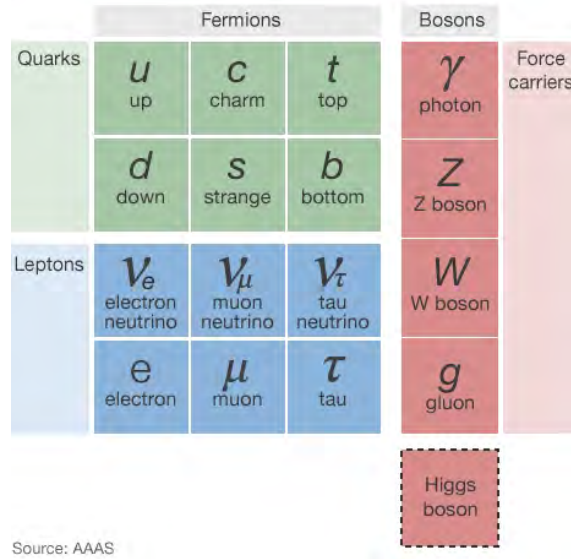
Figure 1.1: The fundamental particles in the SM [1]

SM is a product of the symmetry groups $SU(3) \otimes SU(2) \otimes U(1)$ comprising 2 sectors. The Strong Force (the gauge boson for which is the gluon) is described by the $SU(3)$ sector for Quantum Chromodynamics. The Electromagnetic and Weak Forces (gauge bosons γ and $W^{\pm}$, Z^0) are unified by the $SU(2) \otimes U(1)$ sector for the Electroweak interaction. One of the most significant stumbling blocks of the EW sector to the SM is that the gauge invariance of the $SU(2) \otimes U(1)$ theory leaves no room for mass terms in the Electroweak

3

Lagrangian. Knowing experimentally that $M_W \approx M_Z \approx 100 \times m_{proton}$ the SM exploits the Higgs Mechanism to explain the existence of these masses, at the same time requiring the existence of a new scalar boson, H. It should be noted that the fermions in figure 1.1 have associated antiparticles.

1.1.1 The Electroweak Force

Despite the Electromagnetic and Weak Nuclear Forces appearing to be completely different it was shown independently in 1968 [2][3][4] by Glashow, Salam and Weinburg (GSW) that the two forces are simply two manifestations of the same force - the Electroweak force. The theory is described by the Lagrangian density

$$\mathcal{L}_{EW} = \mathcal{L}_B + \mathcal{L}_W + \mathcal{L}_F + \mathcal{L}_H, \tag{1.1}$$

where $\mathcal{L}_B$ and $\mathcal{L}_W$ represent the kinetic energy of the vector boson fields $W_\mu^i (i = 1, 2, 3)$ and B_μ related to the physical fields of the $W^\pm$, Z^0 and γ. Drawing analogy to the kinetic energy term in Quantum Electrodynamics $(-\frac{1}{4} F_{\mu\nu} F^{\mu\nu}$ where $F_{\mu\nu}$ is the electromagnetic field strength tensor) $\mathcal{L}_B$ and $\mathcal{L}_W$ are given by equations 1.2 and 1.3.

$$\mathcal{L}_W = -\frac{1}{4} \bar{W}_{\mu\nu} . \bar{W}^{\mu\nu} = -\frac{1}{4} \sum \left(\bar{W}_{\mu\nu} \right)^i \left(\bar{W}^{\mu\nu} \right)^i \tag{1.2}$$

$$\mathcal{L}_B = -\frac{1}{4} B_{\mu\nu} . B^{\mu\nu} \tag{1.3}$$

Here $\bar{W}_{\mu\nu} = \partial_\mu \bar{W}_\nu - \partial_\nu \bar{W}_\mu - g \bar{W}_\mu \times \bar{W}_\nu$ and $B_{\mu\nu} = \partial_\mu B_\nu - \partial_\nu B_\mu$. The fermion Lagrangian, $\mathcal{L}_F$, can be split into a quark Lagrangian $\mathcal{L}(q)$ and a lepton Lagrangian $\mathcal{L}(l)$ where

$$\mathcal{L}(l) = \bar{\chi}_L \gamma^\mu \left[i\partial_\mu - g \left(\frac{1}{2} \right) \vec{\tau} . \vec{W}_\mu - \frac{g'}{2} Y(l_L) B_\mu \right] \chi_L + \bar{l}_R \left[i\partial_\mu - \frac{g'}{2} Y(l_R) B_\mu \right] l_R, \tag{1.4}$$

g and g' are the couplings constants, $\vec{\tau}$ the isospin generators (Pauli matrices) and defining the weak isospin doublet

$$\chi_L = \begin{pmatrix} \nu_l \\ l \end{pmatrix}_L \tag{1.5}$$

for each lepton generation e, μ and τ. Similarly for electroweak interactions involving quarks the Lagrangian $\mathcal{L}(q)$ is shown in equation 1.6.

$$\mathcal{L}(q) = \sum_{f=1,2,3} (\bar{\chi}_L^f \gamma^\mu \left[i\partial_\mu - \frac{1}{2} \vec{\tau} . \vec{W}_\mu - \frac{1}{3} B_\mu \right] \chi_L^f) \tag{1.6}$$

where, analogous to the leptonic formulation,

$$\chi_L^f = \begin{pmatrix} U_f \\ D_f' \end{pmatrix}, \ f = 1, 2, 3 \tag{1.7}$$

are $SU(2)$ isospin doublets. Here U corresponds to the up-type quarks u, c and t and D corresponds to the down-type quarks d, s and b. However, since weak interactions are allowed which involve quark flavour transitions between generations ($s \to u$ for example), the weak eigenstates are mixtures of flavour eigenstates, hence D_f' is a mixture of flavour eigenstates according to the CKM (Cabibbo-Kobayashi-Maskawa) rotation matrix.

$$\begin{bmatrix} d' \\ s' \\ b' \end{bmatrix} = \begin{bmatrix} V_{ud} & V_{us} & V_{ub} \\ V_{cd} & V_{cs} & V_{cb} \\ V_{td} & V_{ts} & V_{tb} \end{bmatrix} \begin{bmatrix} d \\ s \\ b \end{bmatrix} = \begin{bmatrix} 0.974 & 0.225 & 0.004 \\ 0.225 & 0.973 & 0.041 \\ 0.009 & 0.040 & 0.999 \end{bmatrix} \begin{bmatrix} d \\ s \\ b \end{bmatrix} \tag{1.8}$$

[5]. The CKM matrix can be parametrised using three angles and a complex phase, the existence of which allows a phenomenon called CP violation. C (Charge Conjugation) interchanges particle and antiparticle. P (Parity) is an inversion of the particle's spatial coordinates. Applying P to a left-handed neutrino would produce a right-handed neutrino. Since in the SM right-handed neutrinos do not exist, P is maximally violated in Weak decays. Also since left-handed anti-neutrinos do not interact in the SM, C is also violated. The combined effect of applying C and P swaps matter for anti-matter. Since the SM allows CP-violation via the complex phase in the CKM matrix, matter and anti-matter do not necessarily behave in the same way.

The GSW formulation of the Electroweak theory does not include mass terms for either fermions or the gauge bosons without breaking the $SU(2) \otimes U(1)$ symmetry. The Electroweak Lagrangian is completed with the inclusion of the Higgs mechanism. By spontaneously breaking the $SU(2) \otimes U(1)$ symmetry with a Higgs field, Φ, with a non-zero vacuum expectation value the underlying physics remains invariant whilst accommodating mass terms in the Lagrangian. The Higgs Lagrangian ($\mathcal{L}_H$) is [6]

$$\mathcal{L}_H = T - V = (D_\mu \Phi)^\dagger D^\mu \Phi - \mu^2 \left(\Phi^\dagger \Phi \right) + \lambda \left(\Phi^\dagger \Phi \right)^2 \tag{1.9}$$

excluding fermionic mass contributions for which Yukawa terms can be added. The form of the potential is chosen such that the vacuum expectation value is non-zero ($\nu = \frac{\mu}{\sqrt{\lambda}}$) and $SU(2) \otimes U(1)$ is spontaneously broken by picking the vacuum from the set of positive minima of the potential V. Expanding the field Φ around this vacuum it is simplest to work in the 'unitary gauge' such that

$$\Phi = \frac{1}{\sqrt{2}} \begin{pmatrix} 0 \\ H + \nu \end{pmatrix}, \tag{1.10}$$

leading to the Higgs Lagrangian

$$\mathcal{L}_H = \frac{1}{2} \partial_\mu H \partial^\mu H + \frac{1}{4} g^2 (H^2 + 2\nu H + \nu^2) W_\mu^+ W^{-\mu}$$
$$+ \frac{1}{8} (g^2 + g'^2)(H^2 + 2\nu H + \nu^2) Z_\mu Z^\mu - \mu^2 H^2 - \frac{\lambda}{4}(H^4 + 4\nu H^3). \tag{1.11}$$

where the masses of the $W^\pm$ and Z can be expressed as

$$M_W = \frac{1}{2} g \nu, \tag{1.12}$$

$$M_Z = \frac{1}{2} \sqrt{(g^2 + g'2)} \nu. \tag{1.13}$$

Furthermore the mass of the Higgs boson itself is $M_H = \sqrt{2}\mu$.

1.1.2   The Strong Force

The $SU(3)$ sector of the SM is described by Quantum Chromodynamics (QCD), a non-abelian gauge theory of interactions between quarks and gluons. As the name suggests, quarks and gluons carry and conserve a colour charge. There are three hypothetical colours - red, green and blue. As a consequence of the non-abelian nature of QCD, unlike in QED where the photon carries no electrical charge, in QCD gluons are colour-charged and consequently can interact with one another. As a result of gluon self-interactions, the coupling in QCD increases as a function of distance. This leads to quarks being confined

within hadrons since at larger and larger separations it becomes energetically favourable for quark-antiquark pairs to be produced rather than quarks themselves becoming isolated. In contrast to Electroweak interactions, QCD couples equally to left- and right-handed quarks and conserves quark flavour.

1.1.3 Unanswered Questions

Despite the success of the SM, there are certain aspects that raise questions about the completeness of the theory. As we have seen in the above summary of the SM, there are many parameters involved. In total there are 25 parameters in the SM, at least 19 of which are completely independent and not predicted. Could there be some underlying symmetry or theory relating some or all of these parameters? The fact that we have to include an ad hoc mechanism to explain the masses of some particles, a mechanism which introduces a new scalar particle (and more parameters) without predicting its own mass is uncomfortable. The existence of three generations of fermions in the SM is also unexplained. CP violation allows matter and anti-matter to behave very slightly differently but there is not enough CP violation in the SM to explain why the universe is made entirely of matter. Finally, where does gravity fit into the SM? As far as particle physics is concerned, gravity has absolutely no effect on the interactions that take place. How can the theory of everything not include a fundamental force like gravity? The existence of these questions and many more alike drive the search for so called New Physics (NP).

1.2 Physics Goals of LHC

The LHCb detector is one of the four main particle physics detectors at the Large Hadron Collider (LHC) at CERN. With a circumference of 27km, the LHC is the world's largest particle physics accelerator designed to accelerate protons in counter-rotating circular paths up to a centre of mass energy of 14TeV. At four points along the ring, the highly relativistic protons are brought together to collide. The collision points are home to four state of the art particle physics detectors. Thousands of particles can be produced when two protons collide at such high energies and it is the role of the particle physics detector to detect and identify these particles and to make measurements of their energy and momentum in order to reconstruct the fundamental interactions through which they were produced. Along with the LHCb (Large Hadron Collider beauty) detector, LHC is home to the ATLAS (A Toroidal LHC ApparatuS), CMS (Compact Muon Solenoid) and ALICE (A Large Ion Collider Experiment) detectors, all studying the proton collisions at the LHC. For short periods the LHC will also collide lead ions which ALICE, ATLAS and CMS will also study. The LHC aims to test the current understanding of the standard model of particle physics and search for signs of new physics beyond the standard model. The main goal of the LHC will be to answer at least some of the unanswered questions surrounding the SM and to discover the Higgs boson. In fact in July 2012, CERN announced that signs of a new scalar boson had been observed by both CMS and ATLAS experiments with a mass in the range of 125-126GeV [7][8].

1.3 Physics Goals of LHCb

LHCb is not a general purpose physics detector but a purpose built high precision detector focussed on studying heavy flavour physics at the new energies provided by the LHC. The study of heavy flavour at the LHC is extremely interesting and offers the opportunity to

probe beyond the standard model processes at energy scales that stretch well above the current 8TeV centre of mass energy at the LHC. LHCb is studying CP violation and CKM measurements, electroweak decays, soft QCD, quarkonia and rare decays. The aim of these measurements is to study the standard model in more detail, improve measurements on some crucial parameters and to hunt for new physics beyond the standard model. The decay $\Lambda_b \to \Lambda^0 \mu^+ \mu^-$ is an interesting rare decay which offers the chance to test the standard model and probe the existence of extensions to the standard model such as supersymmetry [9].

Chapter 2

The LHCb Detector

The particular goals of LHCb compared to those of the general purpose detectors at LHC are reflected in its layout (Figure 2.1(a)). At the LHC, heavy flavour such as hadrons containing a beauty quark are produced predominantly in the very forward or backward directions (Figure 2.1(b)). The angle θ is defined with respect to the beam axis in the proton proton centre of mass frame. As a result the LHCb detector is a single-arm forward spectrometer with an angular coverage of approximately 10 to 300 mrad [10].

(a) View of LHCb in non-bending plane [10]

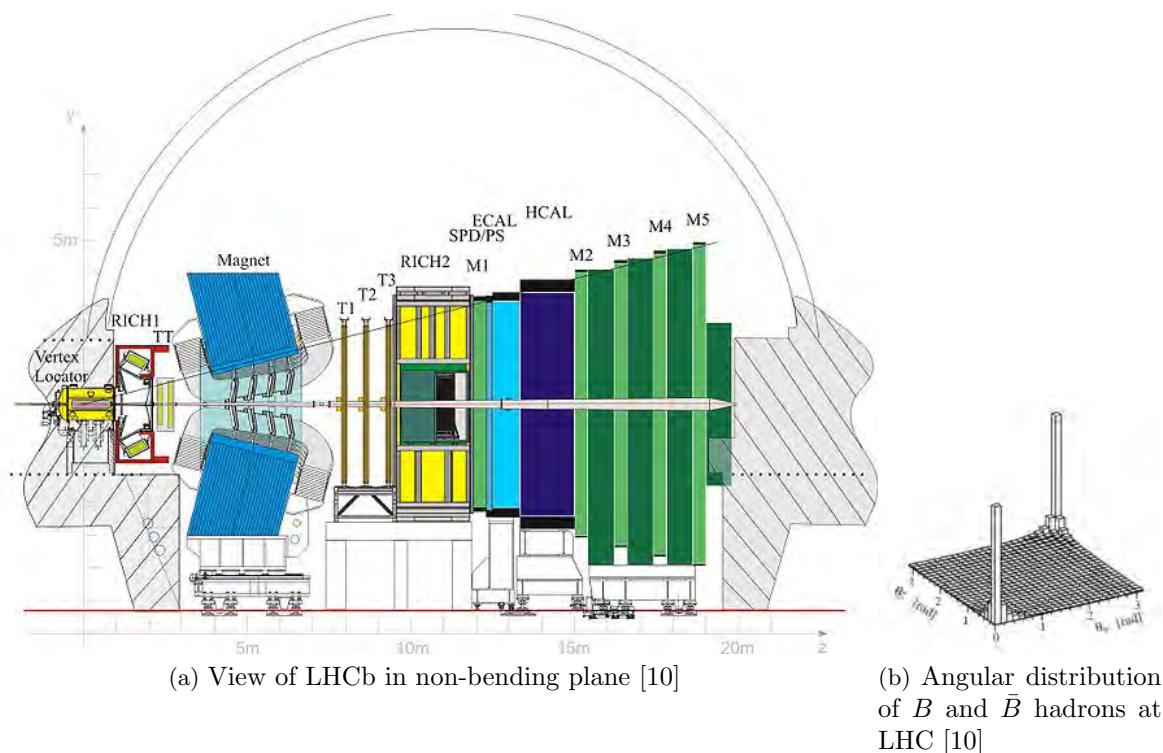(b) Angular distribution of B and $\bar{B}$ hadrons at LHC [10]

Figure 2.1: Layout of LHCb

2.1   Subdetector Components

LHCb's subdetector components are stacked next to each other, starting from the interaction point and continuing outwards in the direction of the beam line. This section briefly summarizes the operation of the LHCb detector in terms of its subdetector components.

2.2 Tracking

2.2.1 Vertex Locator

The Vertex Locator (VELO) provides precise measurements of track coordinates close to the interaction region. Such apparatus is essential in identifying the displaced secondary vertices indicative of the decays of hadrons containing b and c quarks. The VELO covers the angular acceptance of the downstream detectors and is composed of a sequence of silicon modules arranged along the beam line. Each module contains two discs of silicon detectors with circular and radial strips which provide r and ϕ coordinate measurements respectively. The spatial resolution on the vertex location is dependent on the number of tracks in the VELO but is typically around 10μm.

2.2.2 Silicon Tracker

The silicon tracker consists of two detectors, the Trigger Tracker (TT) and the Inner Tracker (IT). The TT is stationed before the LHCb magnet and the IT (consisting of 3 modules) is positioned after the magnet. Both TT and IT use silicon microstrip sensors to measure accurately the track coordinates of charged particles. As charged particles pass through the silicon strips they produce electron-hole pairs. An electric field accelerates the electrons where they are detected as an electric pulse. By using many such microstrips oriented in groups (vertical, $-5°$, $+5°$, vertical) and with the knowledge of which strips have been hit, a very precise position measurement can be made. The silicon trackers have a 50μm single hit resolution.

2.2.3 Outer Tracker

The LHCb outer tracker (OT) is in situ in the same module as the IT but is positioned further away from the beam line (Figure 2.2). The OT employs a different technology in determining track coordinates, employing gas filled straw tubes as a drift-time detector. Whenever a charged particle passes through, it ionizes the gas molecules, producing electrons. The position of the track is found by timing how long the electrons take to reach an anode wire situated in the centre of each tube. The OT has a drift time of less than 50ns and a drift-coordinate resolution of 150μm.

2.3 Magnet

LHCb uses a dipole magnet with an integrated magnetic field of 4Tm in order to measure the momentum of charged particles. The momentum measurement covers the forward acceptance of $\pm$ 250 mrad ($\pm$ 300 mrad) in the non-bending (bending) plane. Track momentum is calculated using the trajectory as determined from the tracking along with knowledge of the magnetic field. The momentum resolution (δp/p) in LHCb is approximately 0.3-0.5%

2.4 RICH System

The RICH (Ring Imaging CHerenkov) detector in LHCb is used to aid particle identification (PID), a fundamental requirement for any particle physics detector. In particular at LHCb it is very important to be able to separate charged hadrons such as pions from kaons in B hadron decays. RICH detectors operate on the principle that charged particles
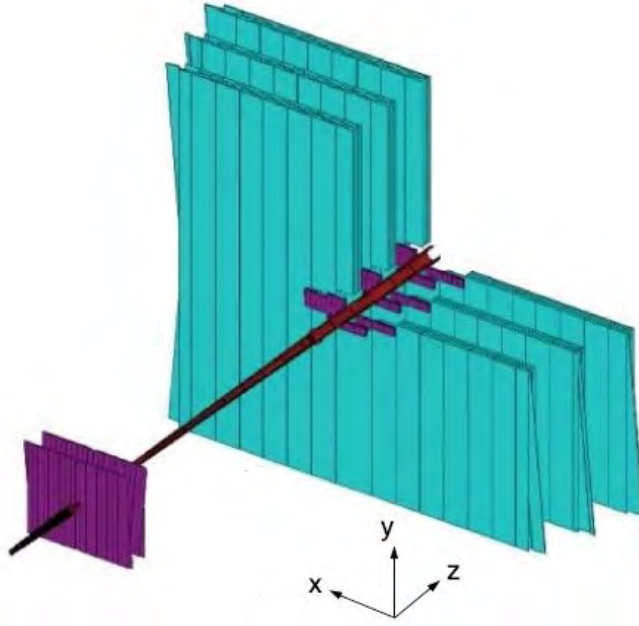
Figure 2.2: TT, IT and OT (blue) [10]

travelling through a refractive medium (a radiator) faster than the speed of light produce Cherenkov radiation. Cherenkov radiation is emitted in a cone and the angle at which the cone of light is produced (θ_c) is related to the mass of the particle traversing the medium. By using arrays of light detectors it is possible to reconstruct the rings of Cherenkov light created in the radiator and calculate a mass hypothesis, hence identifying the particle type. The RICH detector in LHCb must be able to cover the full momentum range of particles and as such there are two RICH systems covering different momentum ranges. RICH 1 is positioned downstream from the VELO, covers the whole LHCb acceptance and contains aerogel and fluorobutane (C_4F_{10}) radiators designed to cover a momentum range of 1–60GeV/c. RICH 2 is positioned between the last tracking station and first muon station. With a CF_4 radiator RICH 2 provides PID from approximately 15 to 100GeV/c. Figure 2.3 shows Cherenkov angle versus particle momentum for the RICH radiators. Both RICH detectors use hybrid photon detectors (HPDs) which measure the spatial positions of emitted Cherenkov photons. All of the HPDs must be shielded from the fringe of the magnetic field of the LHCb dipole.

2.5 Calorimetry

Calorimeters play a vital role in any particle physics detector as they are responsible for measuring the energy of final state particles. Whereas trackers try to measure the coordinates of particles without affecting significantly their energy or momentum, calorimeters are composed of dense materials aimed at completely absorbing incident particles in order to collect their energy. LHCb and indeed most particle physics detectors use both hadronic and electromagnetic calorimeters to measure the energy of hadrons, electrons and photons.
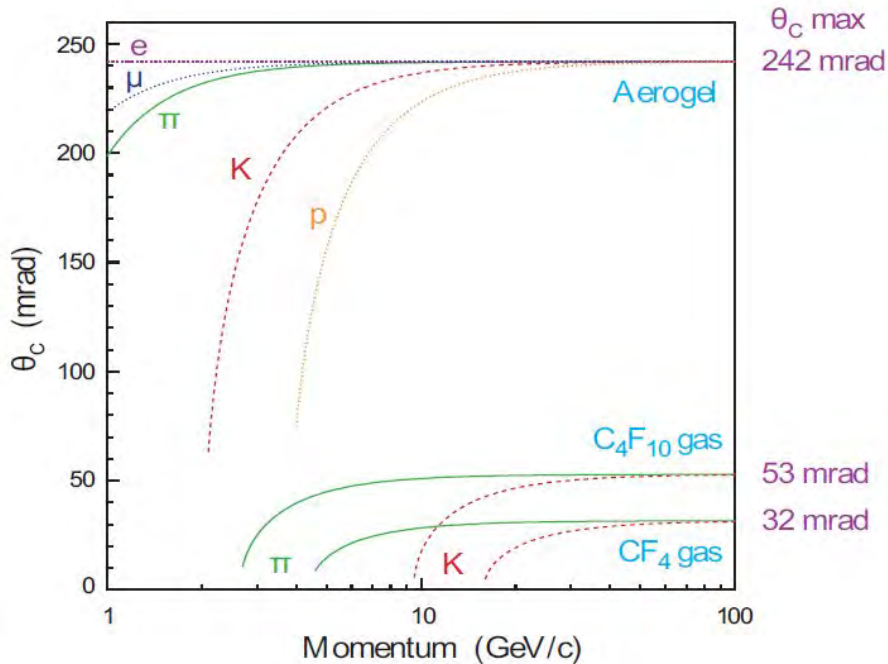
Figure 2.3: Cherenkov angle (θ_c) as a function of momentum for different particle species [10]

2.5.1 Electromagnetic Calorimeter

Electromagnetic calorimeters (ECALs) detect particles which interact via the electromagnetic interaction, predominantly electrons and photons. The LHCb ECAL consists of 2mm layers of lead sandwiched between 4mm layers of scintillator material making a 42cm stack corresponding to 25 radiation lengths (the length over which an incident electron has its energy reduced by a fraction 1/e). As an electron enters the absorbing medium of the ECAL it experiences Coulomb scattering and radiates photons. Photons may then pair produce electron positron pairs which in turn can radiate more. Quickly an electromagnetic shower of secondary electrons, positrons and photons is produced. Scintillator material is then used to convert the shower of particles into UV light. A series of fibres runs through the tiles of lead and scintillator to collect the light and transport it to photomultiplier tubes. By collecting all of the scintillator light in the photomultiplier tubes it is possible to infer the energy of the incoming particle. Similarly, as a photon enters the ECAL, there are three main ways in which it can interact with matter; pair production, Compton scattering and the photoelectric effect. At high energies it is pair production and Compton scattering processes which dominate and these quickly lead to electromagnetic showers.

2.5.2 Hadronic Calorimeter

Hadronic calorimeters (HCALs) work in the same way as ECALs except for detecting particles which interact predominantly via the strong nuclear force. The LHCb HCAL consists of 17cm layers of iron and scintillating tiles. Hadrons entering the HCAL will interact in the iron and produce showers of secondary particles. Charged hadrons interact electromagnetically as well as via the strong nuclear force leading to hadronic showers having both hadronic and electromagnetic components. The HCAL tiles are much larger than the ECAL tiles as the typical nuclear interaction length (mean free path of a particle

without interacting) in a dense material is much larger than the typical radiation length. As with the ECAL, fibres are used to transport the scintillation light to photomultiplier tubes where the particle energy is reconstructed.

2.6 Muon System

Muons interact via the electromagnetic force but due to their large mass do not scatter as readily as electrons. As a result muons are very penetrative and on average will travel through all of the LHCb calorimetry without being absorbed. The LHCb muon system consists of 5 stations containing a total of 1368 Multi Wire Proportional Chambers (MW-PCs). The first muon station is situated before the calorimeters and the remaining four are placed after the calorimeters and separated by 80cm thick iron absorbers to only select very penetrative muons. In general a MWPC uses an anode, which runs through a metal or conductive enclosure whose walls are held at ground potential. The enclosure is filled with gas ($Ar/CO_2/CF_4$ for LHCb), such that any ionizing particle that passes through the tube will ionize the gas. The ionization ions and electrons are accelerated by the electric field around the wire, instigating a cascade of ionization which is collected on the wire and results in an electric current proportional to the energy of the detected particle.

2.7 Triggering

The LHC is designed to provide around 40 million proton collisions every second, although the majority of the data sample used for this analysis was taken at around 20 million collisions every second. LHCb only sees around 10 million events that decay within its geometric acceptance every second. It is not possible to fully reconstruct all 10 million events per second, in fact the total output rate of the detector is around 2000 events per second. In order to make such a reduction in rate it is necessary to keep only the events of particular interest, discarding the rest. The large reduction in rate is achieved by triggering in two levels. The first level (L0) takes information from the VELO, calorimeters and the muon system to reduce the rate from 10MHz to 1MHz. At this point the detector output is sent to a large computing farm where the higher level trigger (HLT) cuts the rate down further from 1MHz to 2kHz. HLT consists of two steps, HLT1 and HLT2.

2.7.1 L0

The L0 trigger is implemented in custom electronics, and is subdivided into three components: the pile-up system, the L0 calorimeter trigger and the L0 muon trigger. B meson decays commonly produce particles with large transverse momentum (p_T) and large transverse energy (E_T). Correspondingly the L0 calorimeter trigger attempts to reconstruct the highest E_T hadron, electron and photon clusters. The L0 muon trigger looks for the two highest p_T muons in the muon chambers. Events are rejected based on global quantities (global event cuts) such as the total energy observed in the calorimeters, the number of tracks and the estimated number of proton proton primary collisions in the VELO. With this information the L0 trigger is able to cut the event rate by 90% whilst being fully synchronised with the 40MHz bunch crossing rate of the LHC.

2.7.2 HLT1

HLT utilises a C++ application which runs on roughly 2000 16-core computing nodes. HLT1 has access to all data in each event and works to further filter events of high

interest. B decays have a relatively long lifetime ($\sim 10^{-12}$ s) and as such B mesons can travel up to a centimetre before decaying. B decay vertices can therefore be characterised as having a high impact parameter with respect to the proton-proton primary vertex. By taking information from the tracking stations and the VELO, HLT1 is able to calculate the impact parameter of particles with respect to the proton-proton vertex and select only B decay candidates. HLT1 reduces the rate to around a few tens of kHz.

2.7.3   HLT2

An offline track reconstruction is performed on the (suitably low rate) output from HLT1 and composite particles are formed. The HLT2 stage then uses cuts on invariant mass or on pointing of the B momentum towards the primary vertex in order to reduce the rate further down to 2kHz.

2.8   Software And Analysis

There is still a lot of data processing required before being able to analyse data from a particle physics detector as part of a physics analysis, and LHCb is no different. The raw data from the machine must be reconstructed in order to be used. Raw signals from the various detector components such as vertices, tracks and energy depositions are used to piece together events and identify particles. It is not possible to fully reconstruct all events as this poses too high a data challenge in terms of both processing and storage. A procedure called stripping is used to selectively reconstruct only the most interesting events. Stripping is effectively a collection of loose selections which aim to select events of particular interest. Each main physics analysis or working group will have one or multiple stripping lines aimed at selecting the correct events. Only events passing a stripping line will be permanently stored for physics analysis.

2.8.1   Monte Carlo

Monte Carlo data is almost as important as actual data and indeed passes through much of the same processing as real data. An Event generator is used to generate particle physics events based on some initial conditions such as the type of particles being collided and their centre of mass energy. The LHCb detector geometry is modelled in detail and the response of the detector to the generated particles is produced based on a set of physical models. The detector response is then digitized and passes through the same reconstruction and stripping routines as real data. The Monte Carlo data can then be used exactly as real data for the benefit of physics analyses.

Chapter 3

Rare Decays

The decay of an unstable particle to a particular final state occurs with a set probability, a so called branching ratio. Rare decays are classed as decays with a very small ($\mathcal{BR} < 10^{-5}$) or even vanishing branching ratio. Generally decays which cannot progress through simple interactions (tree level processes) or are suppressed or violate conservation laws will be rare. Such decays are of particular interest as they provide an excellent hunting ground for new physics processes beyond the standard model.

3.1 The Decay $\Lambda_b \to \Lambda^0 \mu^+ \mu^-$

A Λ_b is an electrically neutral baryon that contains a b quark and two light quarks (ud). With a lifetime of $\tau = 1.4 \times 10^{-12}$s and a mass of $5620 MeV$ with the exception of the extra quark Λ_bs are very similar to B mesons. The Λ^0 is a neutral baryon containing an s quark and two light quarks (ud). With a mass of $1116 MeV$ it decays predominantly in one of two ways,

1. $\Lambda^0 \to p\pi^- \approx 64\%$,

2. $\Lambda^0 \to n\pi^0 \approx 36\%$.

Due to the difficulty of reconstructing events with neutral particles, this decay will only be considered for the cases where the Λ^0 decays to charged particles. The decay $\Lambda_b \to \Lambda^0 \mu^+ \mu^-$ is a rare decay ($\mathcal{BR} \approx 10^{-6}$) and involves the change in flavour of a quark ($b \to s$) without a change in its electric charge. Such processes are called flavour changing neutral currents (FCNCs). FCNCs are forbidden at tree level as they must progress via more complicated interactions. The Feynman diagram in Figure 3.1 shows one such way in which this decay may proceed. The decay $\Lambda_b \to \Lambda^0 \mu^+ \mu^-$ has already been observed by the CDF experiment [17]. FCNCs are interesting because the processes through which they occur are sensitive to contributions from new physics.

3.1.1 Theory

Forward-Backward Asymmetry

The decay $\Lambda_b \to \Lambda^0 \mu^+ \mu^-$ and in general $b \to s$ transitions provide a good test of the standard model and new physics. In such processes the forward-backward asymmetry of the muons in the dimuon rest frame as a function of dimuon invariant mass (q^2) is an important experimentally-observable quantity. Defining $\hat{s} = \frac{q^2}{M_{\Lambda_b}^2}$ and $\hat{m}_b = \frac{m_b}{M_{\Lambda_b}}$ the
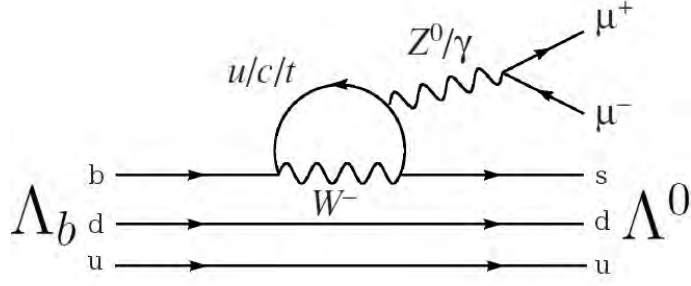
Figure 3.1: Feynman diagram for the decay $\Lambda_b \to \Lambda^0 \mu^+ \mu^-$

differential forward-backward asymmetry is

$$\frac{dA_{FB}(\hat{s})}{d\hat{s}} = \left[\int_0^1 dcos(\theta) \frac{d^2\Gamma(\hat{s})}{d\hat{s}dcos(\theta)} - \int_{-1}^0 dcos(\theta) \frac{d^2\Gamma(\hat{s})}{d\hat{s}dcos(\theta)} \right] \tag{3.1}$$

where θ is the angle the μ^+ makes with respect to the Λ_b^0. Γ is the decay width, and A_{FB} is controlled by three co-efficients; C_7^{eff}, C_9^{eff} and C_{10} [11]. Fig 2. Shows A_{FB} as a function of $\hat{s}$. According to standard model predictions [12], a zero point in A_{FB} is
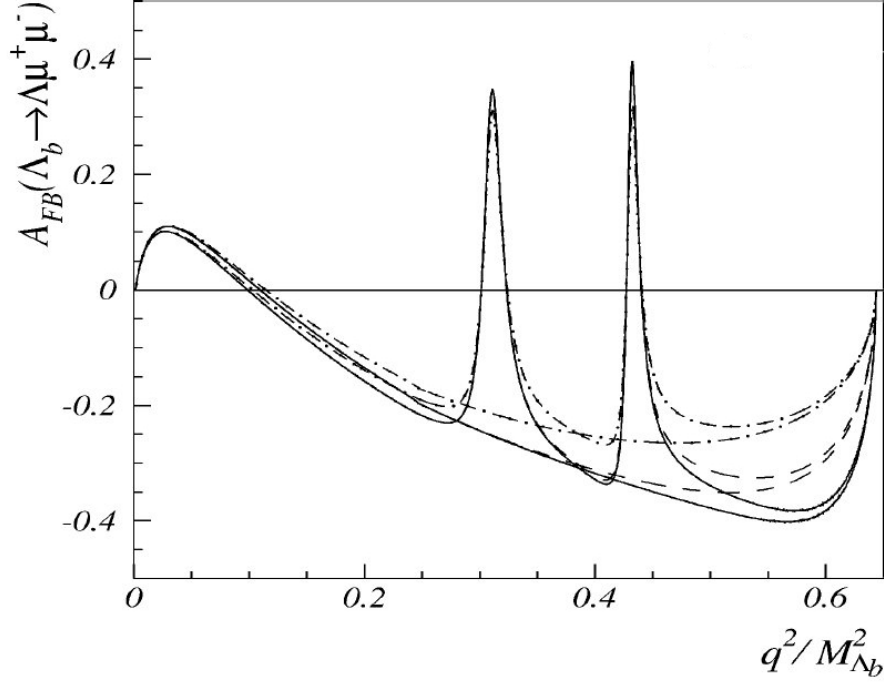
Figure 3.2: A_{FB} of muons in dimuon rest frame [12]. The curves with resonant shapes include long distance contributions and the curves without resonant shapes ignore long distance contributions. The solid curves show the QCD sum rule approach and the dashed (dashed-dotted) show the pole model including (independent of) terms in R (the ratio of the two independent hadronic form factors).

predicted at $\hat{s}_0$, which constrains two of the coefficients such that

$$\Re \left(C_9^{eff} (\hat{s}_0) \right) \simeq - \frac{2\hat{m}_b}{\hat{s}_0} C_7^{eff}. \tag{3.2}$$

15

C_7^{eff} is the effective co-efficient of the electromagnetic penguin operator describing the decay in figure 3.1, the magnitude of which is constrained by the experimental measurements of the $B \to X_s\gamma$ branching ratio which at the 95% confidence level is [13]

$$3.03 \times 10^{-4} < \mathcal{BR}\left(B \to X_s\gamma\right) < 4.07 \times 10^{-4}. \tag{3.3}$$

The bounds on the inclusive radiative $b \to s$ transition rate lead to an uncertainty on the magnitude of C_7^{eff} of

$$0.3 \lesssim |C_7^{eff}(m_B)| \lesssim 0.4. \tag{3.4}$$

From (3.2) the signs of C_7^{eff} and C_9^{eff} are related by

$$sign\left(C_7^{eff}\Re\left(C_9^{eff}\right)\right) = -1. \tag{3.5}$$

It follows that if either one of C_7^{eff} or C_9^{eff} were to have opposite sign to that predicted by the SM, then (3.2) would not be satisfied. Therefore measuring what the authors of [12] quote as a 'sizeable' A_{FB} in this region would be a clear sign of new physics. Some beyond the standard model predictions do exist which involve $sign\left(C_7^{eff}\Re\left(C_9^{eff}\right)\right) = 1$. For example in some supersymmetric models it is possible for C_7^{eff} to be positive or negative and of magnitude within the experimental limits in (3.4).

Λ^0 Polarization

Another observable sensitive to new physics is the polarization of the Λ^0 as this is sensitive to right-handed couplings, which are suppressed in the standard model [14]. The theoretical prediction for the longitudinal polarization asymmetry is shown in Figure 3.3. The longitudinal polarization asymmetry is defined as

$$P_L = \frac{d\Gamma(\hat{e}_L.\hat{\xi} = 1) - d\Gamma(\hat{e}_L.\hat{\xi} = -1)}{d\Gamma(\hat{e}_L.\hat{\xi} = 1) + d\Gamma(\hat{e}_L.\hat{\xi} = -1)}, \tag{3.6}$$

where $\hat{\xi}$ is a unit vector along the Λ^0 spin and $\hat{e}_L$ is a unit vector along the longitudinal component of the Λ polarization. It is important to note that the prediction in Figure 3.3 does not include any contributions from right-handed currents and any such contributions could have an observable effect on the distributions.

3.1.2 Decay Topology

Before discussing how to select $\Lambda_b \to \Lambda^0\mu^+\mu^-$ decays it is useful to consider the topology of the decay and how it will be detected in LHCb. The Λ^0 is a relatively long lived particle with a lifetime of $\tau = 2.6 \times 10^{-10}s$. An average momentum (2GeV/c) Λ^0 will typically travel 3m before decaying. As a result most of the the Λ^0s produced in LHCb will not decay in the VELO but further into the detector, meaning that the tracks used to reconstruct the majority of Λ^0s will not have been reconstructed from hits in all of the tracking stations VELO, TT and IT/OT. The classes of track are defined as follows (see figure 3.4).

- **Long (L) tracks** are reconstructed with hits in all of the LHCb tracking stations. Generally (L) tracks have good momentum resolution and impact parameter resolution.
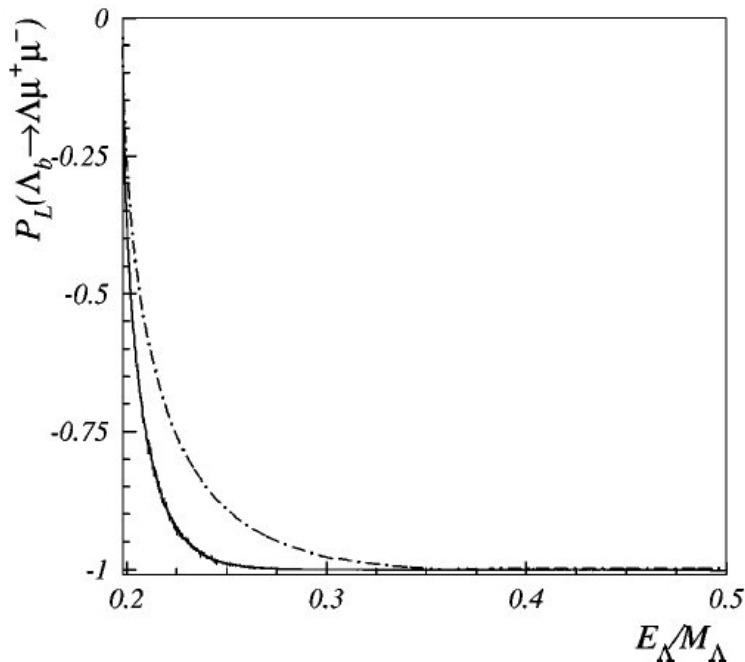
Figure 3.3: Longitudinal polarization asymmetry of Λ^0 [12]. Same legend as figure 3.2. E_Λ and M_Λ are the energy and mass of the Λ^0.

- **Upstream (U) tracks** have hits in only the VELO and TT stations and usually correspond to low momentum particles.

- **Downstream (D) tracks** leave no hits in the VELO and traverse only the TT and T stations (IT or OT). (D) tracks are predominantly from the decay of longer lived particles such as K_S^0 and Λ^0, where they have not decayed in the VELO.

- **VELO tracks** are reconstructed from hits in only the VELO stations and are usually backward or large angle tracks.
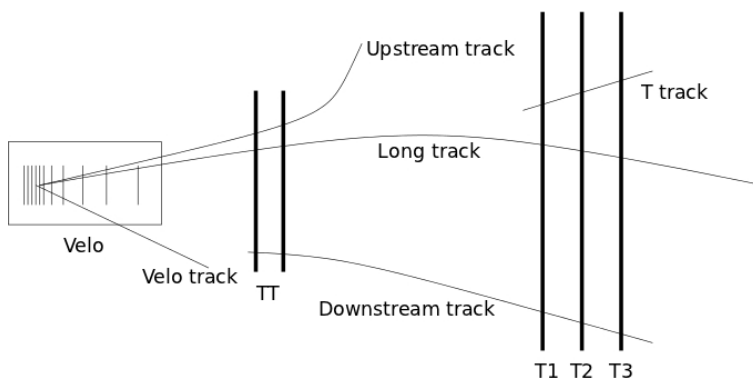

Figure 3.4: Track types in LHCb [10]

The events of interest will require Λ^0s to have been reconstructed from either LL (both tracks are Long) or DD (both tracks are Downstream) tracks, on the grounds that LD (one Long track, one Downstream track) tracks are unphysical, (U) tracks are too low momentum and VELO tracks will have decay products outside of the LHCb geometric

17

acceptance. The disadvantage of long lived particles reconstructed with (DD) tracks is that a vertex for the particle cannot be fitted. Importantly however the true primary vertex can still be determined. The two (DD) tracks can be used to calculate the flight direction of the Λ^0 before decay and this can be used to point backward to a primary vertex in the VELO, provided that the distance travelled by the Λ_b (0.5cm) is negligible compared to that of the Λ^0 (3m).

3.1.3 Experimental Aims and Expected Yield

The initial aim of this analysis is to make an observation of the decay $\Lambda_b \to \Lambda^0 \mu^+ \mu^-$ (which shall be referred to as the 'rare decay') and to measure the branching ratio relative to the control channel $\Lambda_b \to \Lambda^0 J/\psi(1S)$ (the 'resonant decay') where $J/\psi(1S) \to \mu^+\mu^-$. LHCb has yet to observe the rare decay and so far the only official observation of the rare decay is claimed by CDF [17]. For LHCb the aim is not only to observe the rare decay but to study A_{FB} and the differential branching ratio as a function of q^2, as well as study P_L. In order to know how realistic a goal this is, it is necessary to estimate how many $\Lambda_b \to \Lambda^0 \mu^+ \mu^-$ events LHCb can observe for a given integrated luminosity. The expected yield is given by

$$S = N_{\Lambda_b} \times \mathcal{BR}(\Lambda_b \to \Lambda^0 \mu^+ \mu^-) \times \mathcal{BR}(\Lambda^0 \to p\pi^-) \times \epsilon_{tot} \tag{3.7}$$

where

$$N_{\Lambda_b} = L_{int} \times \sigma_{b\bar{b}} \times 2 \times f_{\Lambda_b} \tag{3.8}$$

is the number of expected Λ_b given an integrated luminosity L_{int}, $b\bar{b}$ production cross section $\sigma_{b\bar{b}}$ and Λ_b fragmentation fraction f_{Λ_b} (the fraction of $b\bar{b}$ pairs which fragment to form a Λ_b^0). The factor of 2 takes into account the production of both Λ_b and $\bar{\Lambda}_b$ baryons. ϵ_{tot} is the total efficiency of detection, reconstruction and selection of signal events. With data taken in 2010 at $E_{CM} = 7TeV$, the $b\bar{b}$ production cross section at LHCb was calculated to be $75 \pm 5.4 \pm 13\mu$b [15] and $f_{\Lambda_b} \approx 0.4$ [16]. Therefore $1fb^{-1}$ of LHCb data contains $\approx 6 \times 10^{10}$ Λ_bs. With a branching ratio $\mathcal{BR}(\Lambda_b \to \Lambda^0 \mu^+ \mu^-) = (1.73 \pm 0.42 \pm 0.55) \times 10^{-6}$ [17] and $\mathcal{BR}(\Lambda^0 \to p\pi^-) = 0.639 \pm 0.05$ the expected yield as a function of ϵ_{tot} is

$$S \approx 1 \times 10^5 \times \epsilon_{tot} \tag{3.9}$$

per fb^{-1}. In order to estimate ϵ_{tot} it is useful to consider the very similar decay of $\Lambda_b \to \Lambda^0 J/\psi$ where $J/\psi \to \mu^+\mu^-$. This decay has a branching ratio (in terms of f_{Λ_b}) of $\mathcal{BR}(\Lambda_b \to \Lambda^0 J/\psi) \times f_{\Lambda_b} = (4.7 \pm 2.3) \times 10^{-5}$ and in 2010 LHCb observed 279 ± 19 signal events of this decay with $35pb^{-1}$ of integrated luminosity [18]. Due to the similar topology of these two decays the total detection efficiencies should be broadly similar and the total yield observed in this analysis can be used as an approximate method of estimating ϵ_{tot}. Using equation 3.7 for this case gives $\epsilon_{tot} \approx 0.3\%$. Assuming the same total efficiency, LHCb can expect to see

$$S \approx 100 \tag{3.10}$$

$\Lambda_b \to \Lambda^0 \mu^+ \mu^-$ signal events per $1fb^{-1}$ of integrated luminosity. It must be stated that this calculation is performed ignoring the large errors on $\sigma_{b\bar{b}}$, f_{Λ_b}, $\mathcal{BR}(\Lambda_b \to \Lambda^0 \mu^+ \mu^-)$ and the number of J/ψ events. As such this result is only an order of magnitude approximation. Even so with around 100 signal events observed per fb^{-1} (compared with 24 signal events in $6.8fb^{-1}$ in [17]) it will be possible to observe the rare decay and to measure the branching ratio of the rare decay relative to the resonant decay.

3.1.4 Relative Branching Ratio Measurement

The branching ratio of $\Lambda_b \to \Lambda^0 \mu^+ \mu^-$ will be measured relative to the resonant decay of $\Lambda_b \to \Lambda^0 J/\psi(1S)$ where $J/\psi(1S) \to \mu^+ \mu^-$ since any first order systematic uncertainties common to both decays will cancel out. In order to measure the branching ratio of the rare decay relative to the resonant decay there are many quantities to be determined. Clearly the relative branching ratio is proportional to the relative yields of both decays and the relative efficiencies to select these events through the various stages of detector operation. The complete measurement is given by

$$\mathcal{R} = \frac{\mathcal{BR}(\Lambda_b \to \Lambda \mu^+ \mu^-)}{\mathcal{BR}(\Lambda_b \to J/\psi \Lambda)} = \frac{N_{\Lambda\mu\mu}}{N_{J/\psi\Lambda}} \times \mathcal{BR}(J/\psi \to \mu^+ \mu^-) \times \frac{\epsilon_{J/\psi\Lambda}}{\epsilon_{\Lambda\mu\mu}} \qquad (3.11)$$

where the overall efficiency can be broken down as

$$\frac{\epsilon_{J/\psi\Lambda}}{\epsilon_{\Lambda\mu\mu}} = \frac{\epsilon_{J/\psi\Lambda}^{REC}}{\epsilon_{\Lambda\mu\mu}^{REC}} \times \frac{\epsilon_{J/\psi\Lambda}^{SEL|REC}}{\epsilon_{\Lambda\mu\mu}^{SEL|REC}} \times \frac{\epsilon_{J/\psi\Lambda}^{TRIG|SEL}}{\epsilon_{\Lambda\mu\mu}^{TRIG|SEL}}. \qquad (3.12)$$

Here ϵ^{REC} includes the geometric acceptance (the fraction of events which are produced within the angular acceptance of the detector) and $\epsilon^{SEL|REC}$ is the stripping and selection efficiency with respect to reconstructed events. The trigger efficiency $\epsilon^{TRIG|SEL}$ is calculated with respect to selected events. The relative yields of rare and resonant decays will be extracted from data, the value of $\mathcal{B}(\Lambda_b \to J/\psi \Lambda)$ will be taken from the Particle Data Group and the efficiencies will be calculated in Monte Carlo.

3.2 Selection

3.2.1 Stripping

The first step in selecting decays at LHCb is called stripping. This process is in place to avoid fully reconstructing events that are not of particular interest. The stripping selection comprises a loose set of demands on particle properties which are hard enough to reject a good amount of background without being overly processor intensive. The decay $\Lambda_b \to \Lambda^0 \mu^+ \mu^-$ is no exception to this process and a summary of the stripping selection for this decay follows.

Requirements of Λ_b:

- $BPVDIRA > 0.999968$ - The cosine of the angle between the momentum of the Λ_b and the direction of flight from the best primary vertex to the decay vertex of the Λ_b. In other words the momentum of the Λ_b should agree with the flight path between primary vertex and decay vertex.

- $BPVIPCHI2 < 9.0$ - The χ^2 of the impact parameter fit on the related primary vertex. This requires that the impact parameter of the Λ_b with respect to the primary vertex is suitably small.

- $BPVVDCHI2 > 100.0$ - The χ^2 of the fit of the distance from the related primary vertex to the decay vertex. This requires that the Λ_b travels some distance before decaying. Λ_bs have a similar lifetime to B mesons and so exhibit the same displaced secondary vertex characteristic.

- $VFASPF(VCHI2/VDOF) < 8.0$ - Applies a χ^2 cut on the fit to the end vertex of the particle. This is a requirement that the tracks of the decay products of the Λ_b extrapolate back to a sensible vertex fit for the decay of the Λ_b.

Requirements of Λ^0

- $ADMASS < 30MeV$ - The absolute mass difference of the Λ^0 compared to the PDG value is below 30MeV.

- $PT > 500MeV$ - The transverse momentum of the Λ^0 is greater than 500MeV.

- Lifetime $> 2ps$ - The Λ^0 is a fairly long lived particle. This cut does not get close to the lifetime of the Λ^0 but is useful in rejecting background events.

Requirements of the muons:

- $TRCHI2DOF < 4$ - The muons have good associated tracks.

- $PIDmu > 0$ - The mass hypothesis from the RICH detector is consistent with a muon.

- $MIPCHI2DV(PRIMARY) > 16$ - The muons have a high impact parameter with respect to the primary vertex.

- $VFASPF(VCHI2/VDOF) < 9$ - This is a cut on the dimuon pair and is a requirement that the tracks of the muons point to a good vertex.

3.2.2 Optimization of selection

A cut-based selection is used to maximise the significance of the signal of the rare decay. The selection is optimized by varying the values of the parameters in the stripping selection in order to maximise $\frac{S}{\sqrt{S+B}}$ where S is the integrated signal yield and B is the integrated background in the region of the upper mass sideband (5690–6000MeV) to the signal in the invariant mass distribution. S is the signal yield estimated using the control channel resonant decay so as to avoid biasing the rare decay signal sample. The parameters of the selection are varied individually and the selection is optimised separately for LL and DD type events. The results of the optimization are displayed in figures 3.5 - 3.7 and summarized in table 3.1. In figures 3.5 - 3.7 the blue markers correspond to DD events and the red markers to LL events. The hatchings show the efficiency of the cut at that value for DD and LL events. In general DD events tend to benefit from a tighter selection than LL events since the background to the DD sample is larger as a result of the difficulty reconstructing these events. The error on $\frac{S}{\sqrt{S+B}}$ is larger for DD events despite the DD sample being roughly twice the size of the LL sample. This is due to the error in the fitting process which has increasing uncertainty with larger backgrounds. In all of figures 3.5 - 3.7, the value of $\frac{S}{\sqrt{S+B}}$ is larger for DD events than LL events since for roughly equal signal and background samples, $\frac{S}{\sqrt{S+B}} \propto \sqrt{N}$. Figure 3.5 demonstrates the behaviour of the key selection parameters for the Λ_b^0. The shapes of the distributions are largely flat with some small promise in cutting tighter on DD events in all variables, although this is somewhat subjective considering the size of the error bars. The fact that the advantage in tightening the cuts is small shows that the stripping selection is almost optimal, particularly for LL events. As with the Λ_b selection, the behaviour of the selection parameters for the Λ^0 in figure 3.6 is largely flat. The most obvious feature is the benefit of requiring the Λ^0 to be
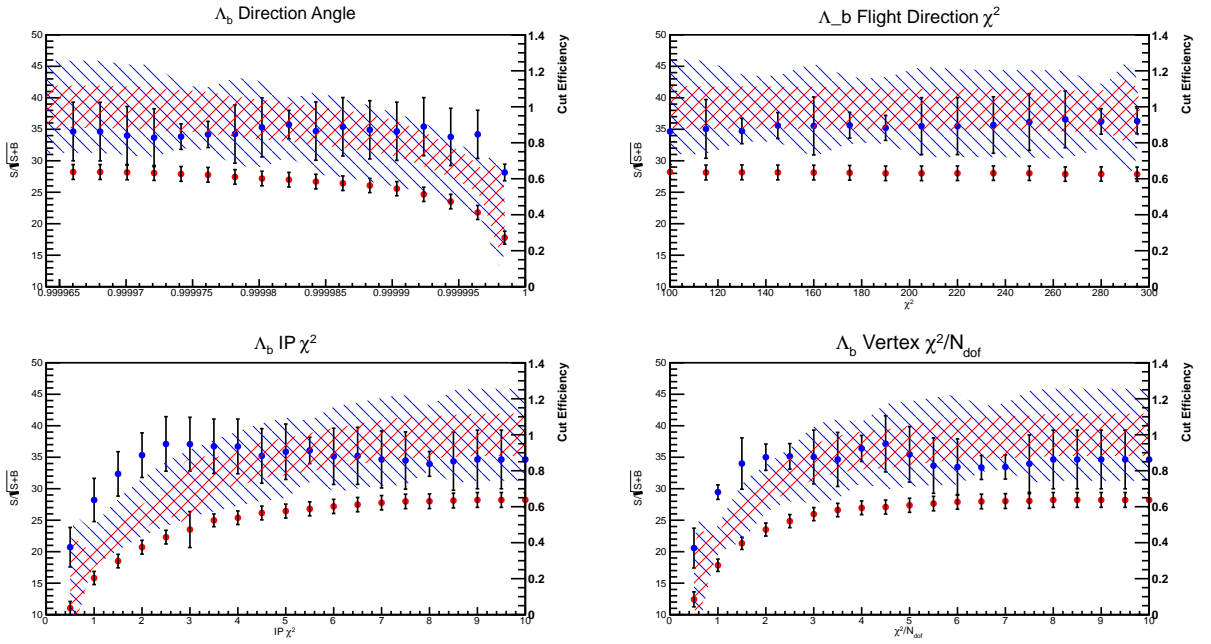
Figure 3.5: $S/\sqrt{S+B}$ as a function of cut value for Λ_b. Top left: BPVDIRA. Top right: BPVVDCHI2. Bottom left: BPVIPCHI2. Bottom right: VFASPF(VCHI2/VDOF). The blue markers correspond to DD events and the red markers to LL events. The hatchings show the efficiency of the cut at that value for DD and LL events

reconstructed from higher momentum DD tracks, since higher momentum Λ^0s will travel further on average before decaying. The bottom right plot in figure 3.6 confirms that the LL events are confined to short-lived Λ^0's. Figure 3.7 shows the variation in selection parameters for the muons in the event. There is little benefit to be had in cutting harder on any of these parameters since the stripping selection is already fairly optimal.

In general the behaviour of the selection variables is fairly flat over a wide range of values. This lack of sensitivity is suggestive of a less than adequate optimization procedure. It should be noted that a multivariate analysis was not used, although there may have been benefit in using one, since a cut-based selection only considers the effect of changing the selection parameters individually and does not consider dependencies between parameters which could enhance the selection. In this cut-based selection, the signal and background samples were not scaled to match the levels of signal and background expected in data, and as a result the sensitivity to varying the parameters is reduced as the value of $\frac{S}{\sqrt{S+B}}$ tends towards $\sqrt{S}$ for a signal dominated sample such as the control channel sample used here.

3.2.3 Triggering

With two muons in the final state, the decay $\Lambda_b \to \Lambda^0 \mu^+ \mu^-$ is readily triggered at L0 by the L0 muon and dimuon triggers, which select events with high momentum or transverse momentum muons. Tracks are filtered according to hits defining a straight line through the five muon stations and pointing towards the interaction point. The most effective HLT1 (High Level Trigger level 1) line for this decay is the Hlt1TrackMuon line. This
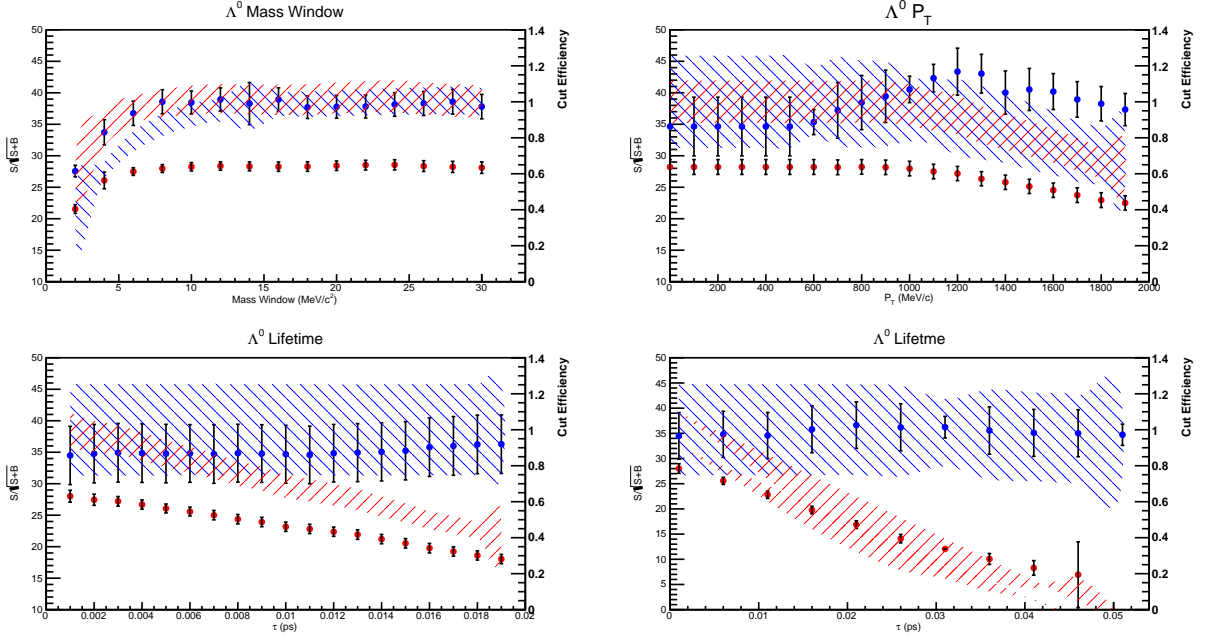
Figure 3.6: $S/\sqrt{S+B}$ as a function of cut value for Λ^0. The blue markers correspond to DD events and the red markers to LL events. The hatchings show the efficiency of the cut at that value for DD and LL events

line is split into two components as it takes as input events which have passed L0Muon or L0DiMuon. The HLT1 line then confirms the muon momentum by reconstructing tracks in the tracking stations, and asserting T tracks extrapolate back to hits in the muon chambers. Depending on whether Hlt1TrackMuon takes input from L0Muon or L0Dimuon and depending on whether single muons are particularly high P_T and whether dimuon combinations are high or low mass, a series of kinematic cuts are employed in order to reduce the rate (Appendix Table A.1). The HLT2 lines used to select events are the HLT2 Single Muon, HLT2 DiMuon Detached, HLT2 Muon Topological and HLT2 Topological lines. The Topological trigger lines look for 2,3 or 4 body events with minimum kinematic requirements on each track. The HLT2 Single Muon line is a continuation of the Hlt1TrackMuon Line with more stringent cuts. The HLT2 DiMuon Detached looks for events with two muons that are displaced from the primary vertex.

3.3   Extracting Efficiencies

The efficiencies associated with track reconstruction, stripping, selection and triggering are required for both channels in order to measure the relative branching ratio of the rare decay to the resonant decay. The efficiencies have been calculated with a sample of Monte Carlo data (MC) emulating the 2011 7TeV running conditions of the LHC. Samples for both the rare and resonant decays were produced from a PYTHIA event generator and the interactions of the particles produced were modelled in the detector geometry before being reconstructed in the same way as real data.
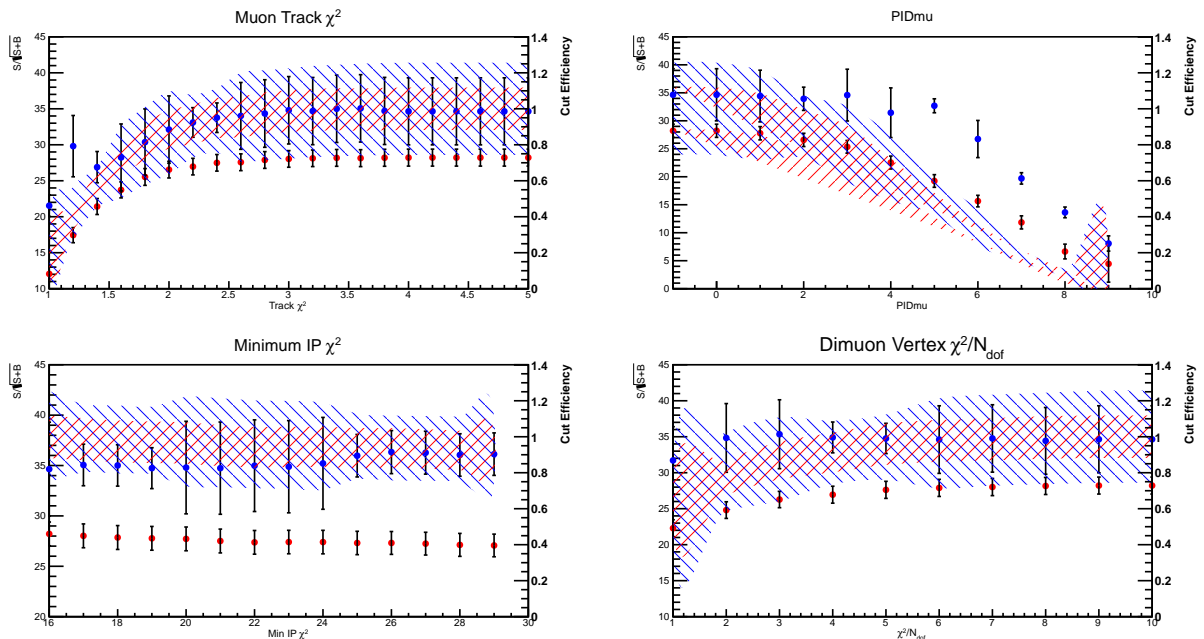
Figure 3.7: $S/\sqrt{S+B}$ as a function of cut value for muons. The blue markers correspond to DD events and the red markers to LL events. The hatchings show the efficiency of the cut at that value for DD and LL events

The final selection parameters are summarized in table 3.1.

3.3.1 Reconstruction

The reconstruction efficiency includes a factor due to the geometric acceptance of the LHCb detector and a factor corresponding to how well the detector is able to reconstruct the tracks of charged particles within its acceptance. Although in reality the reconstruction efficiency and the stripping efficiency are obtained in one step, the reconstruction efficiency has been estimated individually for reference. Table 3.2 shows the fraction of events produced within the LHCb detector acceptance as calculated with generator level MC.

The reconstruction efficiency was estimated by comparing the relative yields of reconstructed versus reconstructible events for both the rare and resonant decays. An event is deemed reconstructible if the decay products leave hits in the appropriate detector components such that they should be reconstructed. For example, consider a rare decay which produces along with two muons a Λ^0 which decays into a proton and a pion both of which are DD. If the muons leave hits in the VELO and T stations and the decay products of the Λ^0 leave hits in the TT and T stations then the decay is deemed reconstructible. Reconstructed events are found simply by exploring the best reconstructed tracks in the MC. This method serves only as an approximation to see the general behaviour of the reconstruction. Table 3.3 lists the reconstruction efficiency for the rare decay as a function of q^2. As would be expected, the reconstruction efficiency of the DD events is poorer than for the LL events. ϵ_{DD}^{REC} reduces as q^2 increases, because in the region of high q^2 where hard muons result in a soft Λ^0, the reconstruction efficiency of the DD events suffers. The LL events demonstrate a fairly flat reconstruction efficiency over all q^2.

23

Stripping and Optimised Selection				
Particle	Variable	Stripping	LL	DD
Λ_b	Mass	$4900 < m < 7000 MeV$	-	-
	BDIRA	> 0.999968	0.999968	0.999978
	$IP\chi^2$	< 9.0	< 8.0	< 7.0
	$FlightDistance\chi^2$	> 100.0	> 130.0	> 180.0
	$Vertex\chi^2/\text{DOF}$	< 8.0	< 5.0	< 4.0
Λ^0	Mwin	$30 MeV$	$20 MeV$	$15 MeV$
	PT	$> 500 MeV$	$> 800 MeV$	$> 1000 MeV$
	Lifetime	$> 2ps$	-	-
Muons	$Track\chi^2/\text{DOF}$	< 4.0	-	-
	PIDmu	> 0	-	-
	$IP\chi^2$	> 16.0	-	-
J/ψ	$Vertex\chi^2/\text{DOF}$	< 9.0	< 9.0	< 8.0
	Mass	$< 5050 MeV$	-	-

Table 3.1: Stripping and Selection Cuts

Geometric Acceptance	
q^2 (GeV^2/c^4) bin	ϵ^{ACC}
$[0.00, 2.00]$	0.14 ± 0.03
$[2.00, 4.30]$	0.15 ± 0.03
$[4.30, 8.68]$	0.13 ± 0.02
$[10.09, 12.86]$	0.11 ± 0.03
$[14.18, 16.00]$	0.15 ± 0.05
$[16.00, 20.30]$	0.13 ± 0.04
$[0.00, 20.30]$	0.13 ± 0.01

Table 3.2: Geometric Acceptance for $\Lambda_b \rightarrow \Lambda \mu^+ \mu^-$ in generator level MC. Excluded regions of q^2 correspond to the $J/\psi(1S)$ and $\psi(2S)$ resonances.

3.3.2 Stripping

The fraction of fully reconstructed events which pass the stripping selection provides the stripping efficiency. In reality the efficiency to strip events is folded together with the reconstruction efficiency as only events passing the stripping selection are recorded. Table 3.4 summarizes the combined reconstruction and stripping efficiency. Knowing the relative shape of the reconstruction efficiency we can decouple the stripping efficiency in table 3.4. The reconstruction efficiency for LL events is flat, meaning that as q^2 increases so does the stripping efficiency. The increase in stripping efficiency for DD events as a function of q^2 is even more marked considering the decrease seen in reconstruction efficiency for increasing q^2.

3.3.3 Selection

The selection efficiency is calculated with MC and is the fraction of events passing the stripping selection which also pass the optimised stripping selection. Table 3.5 summarizes the selection efficiency as a function of q^2 (combined for both DD and LL events).

Reconstruction Efficiency		
q^2 (GeV^2/c^4) bin	ϵ_{LL}^{REC}	ϵ_{DD}^{REC}
[0.00, 2.00]	0.962 ± 0.003	0.774 ± 0.003
[2.00, 4.30]	0.959 ± 0.003	0.764 ± 0.003
[4.30, 8.68]	0.958 ± 0.002	0.738 ± 0.002
[10.09, 12.86]	0.970 ± 0.002	0.711 ± 0.004
[14.18, 16.00]	0.973 ± 0.003	0.677 ± 0.005
[16.00, 20.30]	0.970 ± 0.003	0.647 ± 0.005

Table 3.3: Reconstruction efficiency for $\Lambda_b \to \Lambda \mu^+ \mu^-$ in MC. Excluded regions of q^2 correspond to the $J/\psi(1S)$ and $\psi(2S)$ resonances. The relative number of DD to LL events is $\approx 2:1$

Reconstruction and Stripping Efficiency		
q^2 (GeV^2/c^4) bin	$\epsilon_{LL}^{REC} \times \epsilon_{LL}^{STRIP\|REC}$	$\epsilon_{DD}^{REC} \times \epsilon_{DD}^{STRIP\|REC}$
[0.00, 2.00]	0.023 ± 0.002	0.018 ± 0.001
[2.00, 4.30]	0.030 ± 0.002	0.023 ± 0.001
[4.30, 8.68]	0.029 ± 0.001	0.029 ± 0.001
[10.09, 12.86]	0.039 ± 0.002	0.043 ± 0.001
[14.18, 16.00]	0.040 ± 0.003	0.048 ± 0.002
[16.00, 20.30]	0.040 ± 0.003	0.055 ± 0.002
[0.00, 20.30]	0.032 ± 0.000	0.055 ± 0.002

Table 3.4: Reconstruction and Stripping efficiency for $\Lambda_b \to \Lambda \mu^+ \mu^-$ in MC. Excluded regions of q^2 correspond to the $J/\psi(1S)$ and $\psi(2S)$ resonances.

In contrast to the stripping efficiency, the selection efficiency improves as q^2 decreases. Bearing in mind that the muon selection variables remained unchanged in optimising the overall selection then this behaviour must be attributed to the Λ_B and Λ^0 cuts. The P_T cut on the Λ^0 was increased, selecting more events with low q^2. The mass window on the Λ^0 was also tightened. This means that true Λ^0s with a poor mass resolution, possibly from high momentum DD tracks caused by soft muons, will not be selected. The selection efficiencies for both LL and DD events are shown in figure 3.8. It is clear to see that the efficiency to select LL events remains flat as a function of q^2 whereas the noticeable drop in combined selection efficiency can be attributed to the DD selection.

3.3.4 Triggering

The trigger efficiency is calculated with respect to selected events and calculated using the TISTOS method [22]. The TISTOS method allows trigger efficiencies to be extracted from data or MC from observable variables in the data. The method classifies events depending on how they were actually triggered. Events in which the signal particles fire the trigger (for example two high momentum muons in the decay $\Lambda_b \to \Lambda^0 \mu^+ \mu^-$ triggers the event to be recorded) are classified as 'Triggered On Signal', or TOS. Events in which non-signal particles trigger the event are classified as 'Triggered Independently of Signal', or TIS. Events can be classified as TIS and TOS (TISTOS), where the event was both triggered TIS and TOS, not to be confused with TOB events which are never TIS nor TOS

Combined Selection Efficiency (LL and DD)	
q^2 (GeV^2/c^4) bin	$\epsilon^{SEL\|STRIP}$
$[0.00, 2.00]$	0.870 ± 0.003
$[2.00, 4.30]$	0.881 ± 0.003
$[4.30, 8.68]$	0.883 ± 0.002
$[10.09, 12.86]$	0.864 ± 0.003
$[14.18, 16.00]$	0.831 ± 0.004
$[16.00, 20.30]$	0.778 ± 0.004
$[0.00, 20.30]$	0.861 ± 0.001

Table 3.5: Selection Efficiency for $\Lambda_b \to \Lambda \mu^+ \mu^-$ in MC. Excluded regions of q^2 are $J/\psi(1S)$ and $\psi(2S)$ resonances.

by definition. Since the trigger efficiency is calculated with respect to selected events, we can define the trigger efficiency as

$$\epsilon^{TRIG|SEL} = \frac{N^{TRIG}}{N^{SEL}}. \tag{3.13}$$

In order to calculate the trigger efficiency we require N^{TRIG} which is easily observable in data and N^{SEL} which is not. N^{SEL} is the number of events selected prior to passing the trigger. However if equation 3.13 holds then

$$\epsilon^{TIS} = \frac{N^{TIS}}{N^{SEL}} \tag{3.14}$$

is true for TIS events. The crux of the TISTOS method hinges on the fact that, provided the signal is totally independent of the underlying event, the TIS efficiency ϵ^{TIS} is given by

$$\epsilon^{TIS} = \frac{N^{TISTOS}}{N^{TOS}}. \tag{3.15}$$

Therefore we are able to express the trigger efficiency

$$\epsilon^{TRIG|SEL} = \frac{N^{TRIG}}{N^{SEL}} = \frac{N^{TIS}}{N^{SEL}} \times \frac{N^{TRIG}}{N^{TIS}} = \epsilon^{TIS|SEL} \times \frac{N^{TRIG}}{N^{TIS}} \tag{3.16}$$

$$\epsilon^{TRIG|SEL} = \frac{N^{TISTOS}}{N^{TOS}} \times \frac{N^{TRIG}}{N^{TIS}} \tag{3.17}$$

in terms of variables which are completely observable in the data. Realistically the signal decay will be correlated to the underlying event, but providing the correlation is weak and ϵ^{TIS} remains fairly flat, then the TISTOS method remains an acceptable method. Figure 3.9 shows the trigger efficiency of the L0 triggers as a function of q^2. It is interesting to note that the TIS efficiency is fairly flat and very small compared to the TOS efficiency. The overall efficiency $\epsilon^{TRIG|SEL}$ and the TOS efficiency show very similar behaviour over the entire q^2 region, suggesting as expected that the trigger decisions are dominated by TOS decisions. Figure 3.10 shows the trigger efficiency of the HLT1 triggers as a function of q^2. The TIS efficiency is a little larger in general compared to the L0 triggers. The TIS efficiency also shows more variation as a function of q^2. The errors on the values are only statistical and do not include any bias due to the assumption of a flat TIS efficiency. The overall trigger efficiency of HLT1 is fairly good and well behaved in q^2. Figure 3.11 shows the efficiency of the HLT2 triggers. A variety of trigger lines were used including
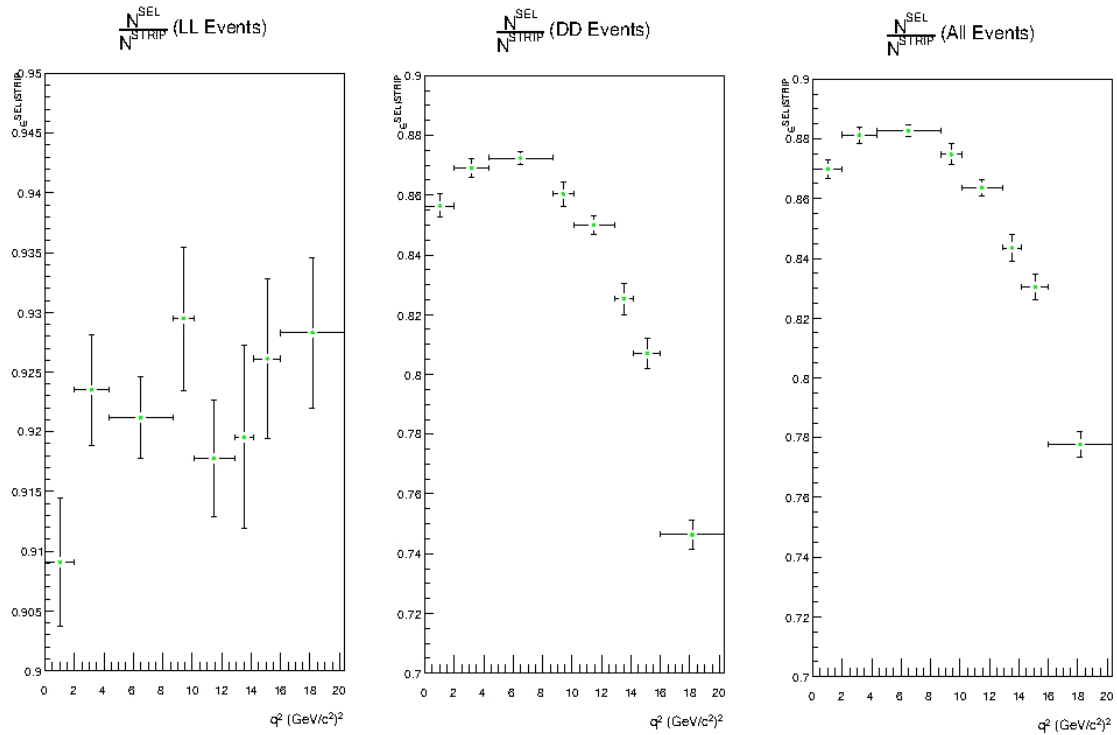
26

Figure 3.8: Selection efficiency for $\Lambda_b \to \Lambda^0 \mu^+ \mu^-$ in MC

topological lines and muon lines. In this instance the TIS efficiency is definitely not flat and will bias the overall efficiency. The HLT2 efficiency shows a gentle increase as a function of q^2. This is a general pattern with muon triggers as high momentum muons are required in order to trigger. The trigger efficiency is boosted in the lower q^2 regions by the topological line which displays a trade off between hard muons and high momentum decay products of the Λ^0. The combined efficiency to trigger on the rare decay is summarized in table 3.6.

Combined Trigger Efficiency (L0, HLT1 and HLT2)	
q^2 (GeV^2/c^4) bin	$\epsilon^{TRIG\|SEL}$
[0.00, 2.00]	0.65 ± 0.15
[2.00, 4.30]	0.69 ± 0.13
[4.30, 8.68]	0.67 ± 0.09
[10.09, 12.86]	0.85 ± 0.15
[14.18, 16.00]	0.86 ± 0.20
[16.00, 20.30]	0.82 ± 0.16
[0.00, 20.30]	0.72 ± 0.05

Table 3.6: Trigger Efficiency for $\Lambda_b \to \Lambda \mu^+ \mu^-$ in MC. Excluded regions of q^2 are $J/\psi(1S)$ and $\psi(2S)$ resonances.

Table 3.6 shows the overall efficiency to trigger on $\Lambda_b \to \Lambda \mu^+ \mu^-$ is quite good and improves with higher q^2. The errors are purely statistical and do not reflect any bias or inherent error from the TISTOS method.
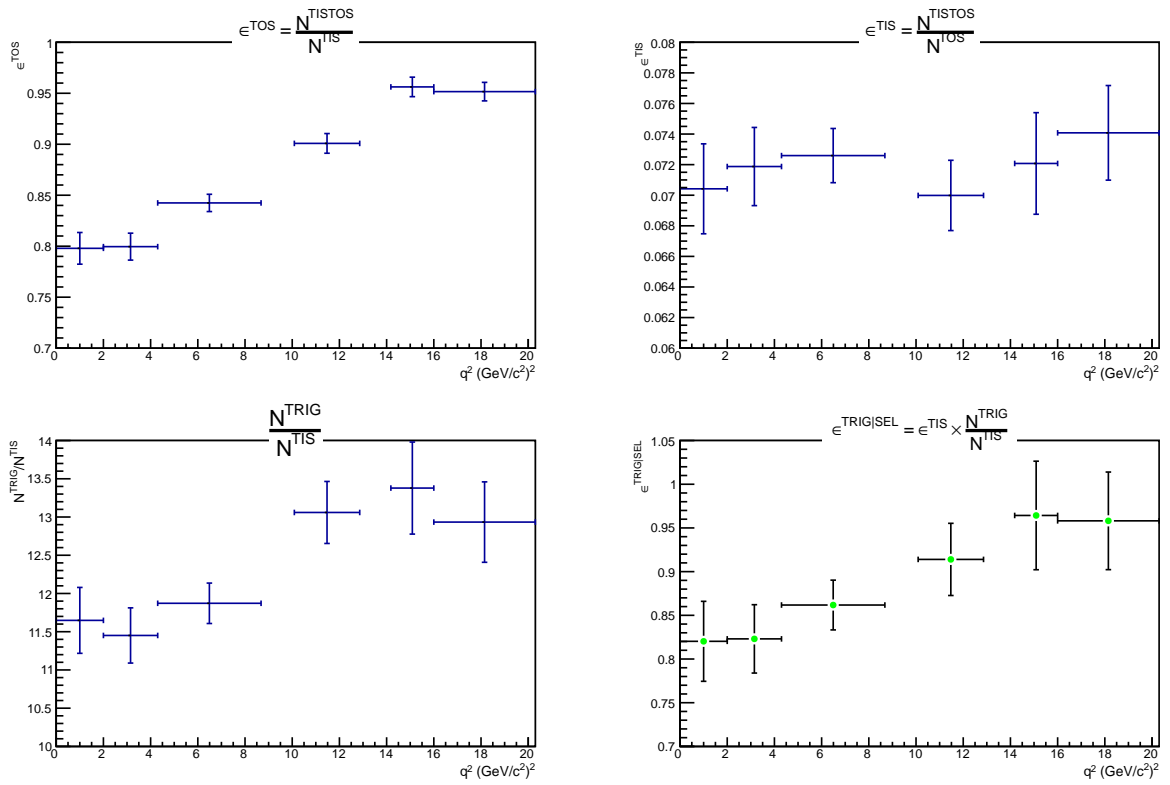
Figure 3.9: The L0 Trigger Efficiency for the rare decay as calculated with MC data. Top Left: $\epsilon^{TOS}(q^2)$, Top Right: $\epsilon^{TIS}(q^2)$, Bottom Left: $\frac{N^{TRIG}}{N^{TIS}}(q^2)$, Bottom Right: $\epsilon^{TRIG|SEL}(q^2)$
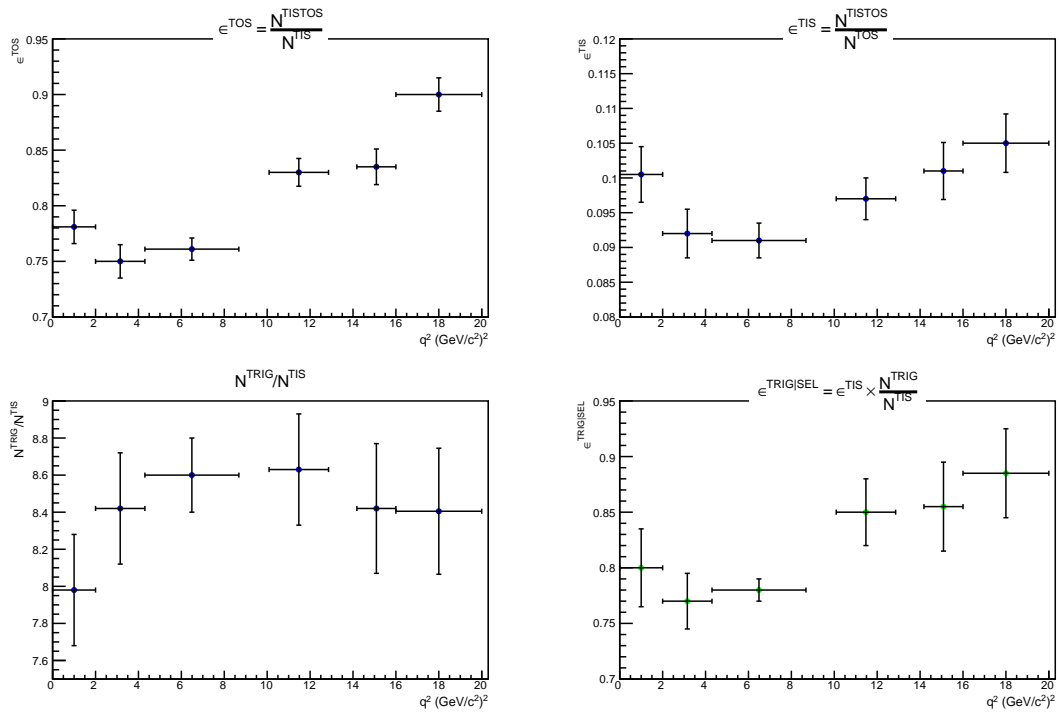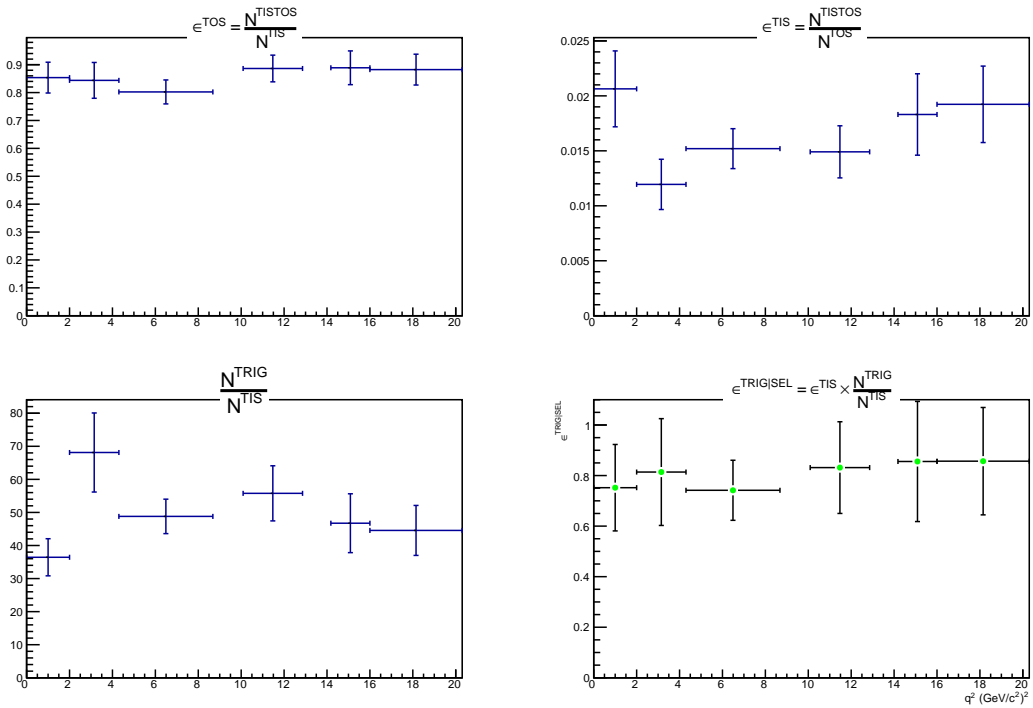
Figure 3.10: The HLT1 Trigger Efficiency for the rare decay as calculated with MC data. Top Left: $\epsilon^{TOS}(q^2)$, Top Right: $\epsilon^{TIS}(q^2)$, Bottom Left: $\frac{N^{TRIG}}{N^{TIS}}(q^2)$, Bottom Right: $\epsilon^{TRIG|SEL}(q^2)$

Figure 3.11: The HLT2 Trigger Efficiency for the rare decay as calculated with MC data. Top Left: $\epsilon^{TOS}(q^2)$, Top Right: $\epsilon^{TIS}(q^2)$, Bottom Left: $\frac{N^{TRIG}}{N^{TIS}}(q^2)$, Bottom Right: $\epsilon^{TRIG|SEL}(q^2)$

Chapter 4

Measurement

In order to calculate the relative branching ratio between the rare and resonant decays (according to equations 3.11 and 3.12) the integrated yields of the two decay channels need to be calculated. The optimised selection was used to select the rare decays and the stripping selection was used to select the resonant decays. Figures (4.1 to 4.4) were fitted with the combination of a quadratic background function and a Gaussian peak. The dataset for these events is the 2011 dataset corresponding to approximately $1fb^{-1}$ of integrated luminosity at a centre of mass energy of 7TeV. Most of the data in the 2011 dataset was recorded when the machine was operating at a 20MHz bunch crossing rate with 1296 bunches. The peak luminosity achieved was almost $4 \times 10^{-32}cm^{-2}s^{-1}$ which is twice the initial design luminosity. Figure 4.1 shows $\Lambda_b \to \Lambda J/\Psi(\to \mu^+\mu^-)$ events from
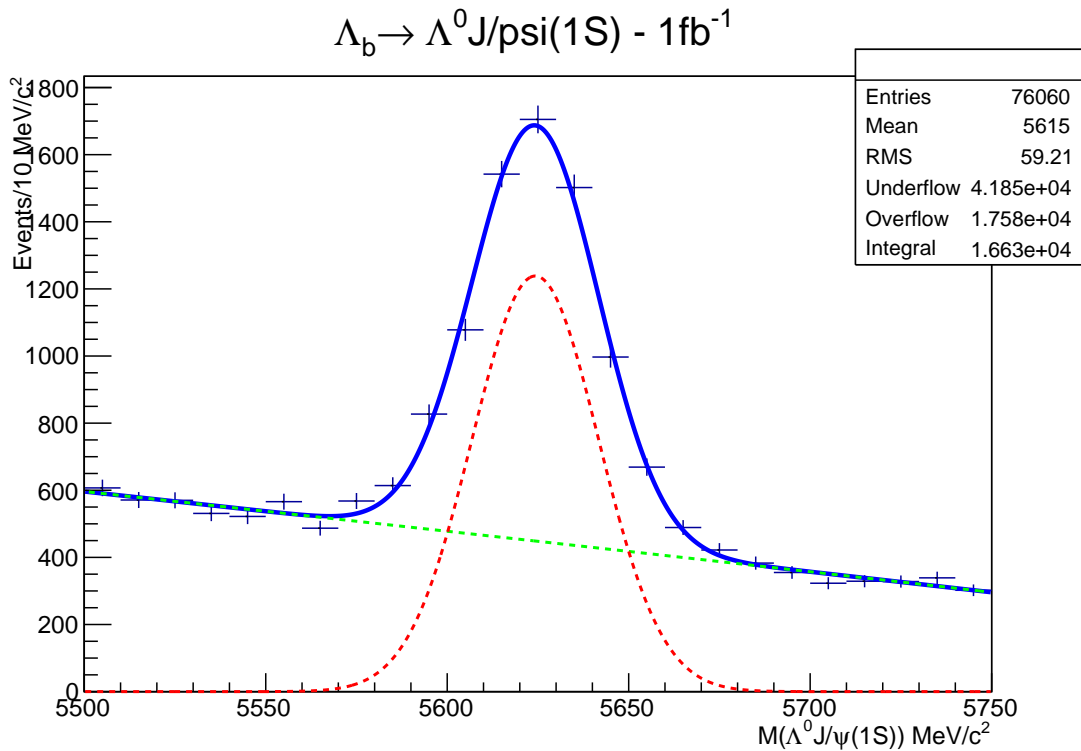

Figure 4.1: Observing the resonant $\Lambda_b \to \Lambda J/\Psi(\to \mu^+\mu^-)$ decay as selected by stripping. The dashed green line is the background function, the dashed red line is the signal function and the solid blue line is the sum of the green and red dashed lines.

stripped data. The background is fairly flat and is fit with a straight line. Even with the loosest selection the signal region is clearly visible over the background. Considering the resonant decay is more abundant it is clear that the selection for the rare decay needs to remove a substantial amount of background in order to see the signal.

Fitting Parameters for Figure 4.1	
Parameter	Value
Background	
Constant	3760.0 ± 169.1
Co-efficient of x	$(2.35 \pm 0.01) \times 10^{-2}$
Co-efficient of x^2	$(-1.09 \pm 0.01) \times 10^{-4}$
Signal	
Height (Events/$10MeV/c^2$)	1238.5 ± 27.0
Mass (MeV/c^2)	5624.3 ± 3.73
Width (MeV/c^2)	17.5 ± 0.4

Table 4.1: Fitting Parameters for Figure 4.1.

According to the PDG, the mass for the Λ_b^0 is $5619.4 \pm 0.7 MeV/c^2$ which is consistent with the result in figure 4.1. Figure 4.2 shows the rare decay events in the LL sample. The background although similar in shape to figure 4.1 is much reduced. The signal is small (integrated 37 events according to fit parameters) and the errors are large. Figure 4.3 shows the rare decay events in the DD sample. As expected the background is much larger, however an enhanced region is visible in the mass window of the Λ_b. Figure 4.4 combines the LL and DD samples in figures 4.2 and 4.3 to see the overall selection of the rare decay in data. According to the fitting of the data, we see approximately 100 $\Lambda_b \to \Lambda \mu^+ \mu^-$ events and 5400 $\Lambda_b \to \Lambda J/\Psi(\to \mu^+ \mu^-)$ events. The significance of the rare decay signal, $\frac{S}{\sqrt{S+B}}$, is calculated using the integrated signal yield in the signal region and the integrated background contribution in the same region. $\frac{S}{\sqrt{S+B}} \approx 4.8\sigma$ which gives some confidence that the signal yield corresponds to the rare decay of $\Lambda_b \to \Lambda \mu^+ \mu^-$ and is not a fluctuation in the background. According to equation 3.11, the relative branching ratio is calculated as

$$\mathcal{R} = \frac{\mathcal{B}(\Lambda_b \to \Lambda \mu^+ \mu^-)}{\mathcal{B}(\Lambda_b \to J/\psi\Lambda)} = \frac{N_{\Lambda\mu\mu}}{N_{J/\psi\Lambda}} \times \mathcal{B}(J/\psi \to \mu^+\mu^-) \times \frac{\epsilon_{J/\psi\Lambda}}{\epsilon_{\Lambda\mu\mu}} = (1.89 \pm 0.32) \times 10^{-3} \quad (4.1)$$

where the error is only statistical, assuming uncorrelated errors. This does not include the error in the fitting which is very large. The systematic uncertainty in the fitting procedure could have been reduced by using different fitting methods. The lower mass sideband may contain peaking backgrounds which add to the uncertainty of the fit. Monte Carlo data could have been used to assess the systematic uncertainty of the fitting procedure of multiple data samples of similarly shaped signal and background.

For the combined fit of figure 4.4 the fitting results gave a yield of 98.2 ± 78.3 signal events and 311.0 ± 14.8 background events in the signal region.
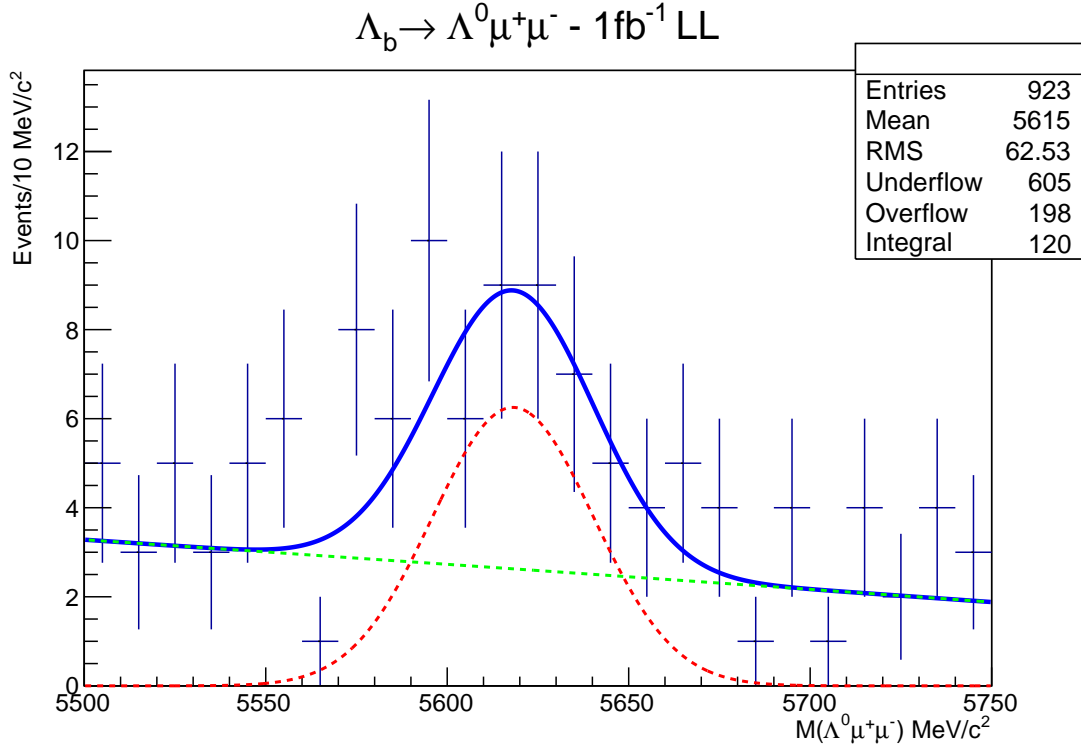
Figure 4.2: Observing the LL contribution to the rare decay $\Lambda_b \to \Lambda \mu^+ \mu^-$ as selected by the optimised LL selection. The dashed green line is the background function, the dashed red line is the signal function and the solid blue line is the sum of the green and red dashed lines.

Fitting Parameters for Figure 4.2-4.4			
Background			
Figure	4.2	4.3	4.4
Constant	18.8 ± 4.7	106.5 ± 5.0	126.2 ± 15.9
Co-efficient of x	$(-1.6 \pm 8.6) \times 10^{-4}$	$(1.5 \pm 2.7) \times 10^{-3}$	$(1.7 \pm 2.9) \times 10^{-3}$
Co-efficient of x^2	$(-4.8 \pm 1.5) \times 10^{-7}$	$(-2.7 \pm 0.5) \times 10^{-6}$	$(-3.2 \pm 0.5) \times 10^{-6}$
Signal			
Figure	4.2	4.3	4.4
Height (Events/$10 MeV/c^2$)	6.3 ± 1.6	15.1 ± 4.4	19.9 ± 4.7
Mass (MeV/c^2)	5618.1 ± 6.3	5623.1 ± 6.0	5261.3 ± 5.1
Width (MeV/c^2)	22.2 ± 4.8	18.7 ± 5.6	19.7 ± 4.6

Table 4.2: Fitting Parameters for Figure 4.2-4.4.

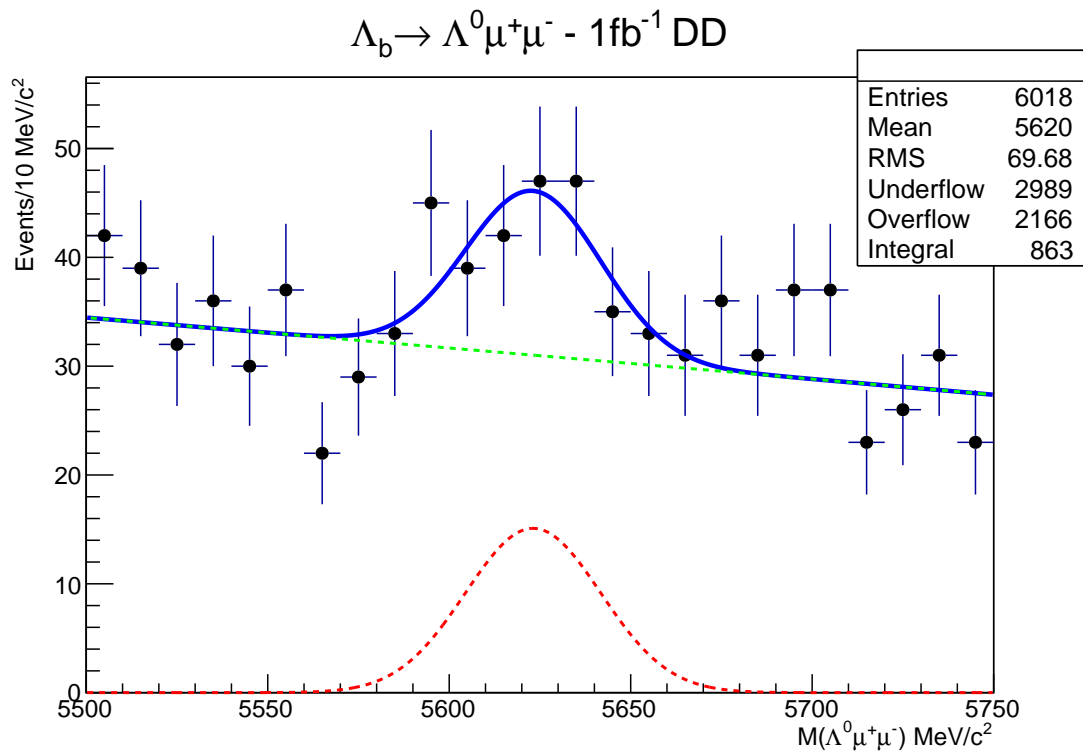Figure 4.3: Observing the DD contribution to the rare decay $\Lambda_b \to \Lambda \mu^+ \mu^-$ as selected by the optimised DD selection. The dashed green line is the background function, the dashed red line is the signal function and the solid blue line is the sum of the green and red dashed lines.

Figure 4.4: Observing the rare decay $\Lambda_b \to \Lambda \mu^+ \mu^-$ (combined LL and DD events). The dashed green line is the background function, the dashed red line is the signal function and the solid blue line is the sum of the green and red dashed lines.
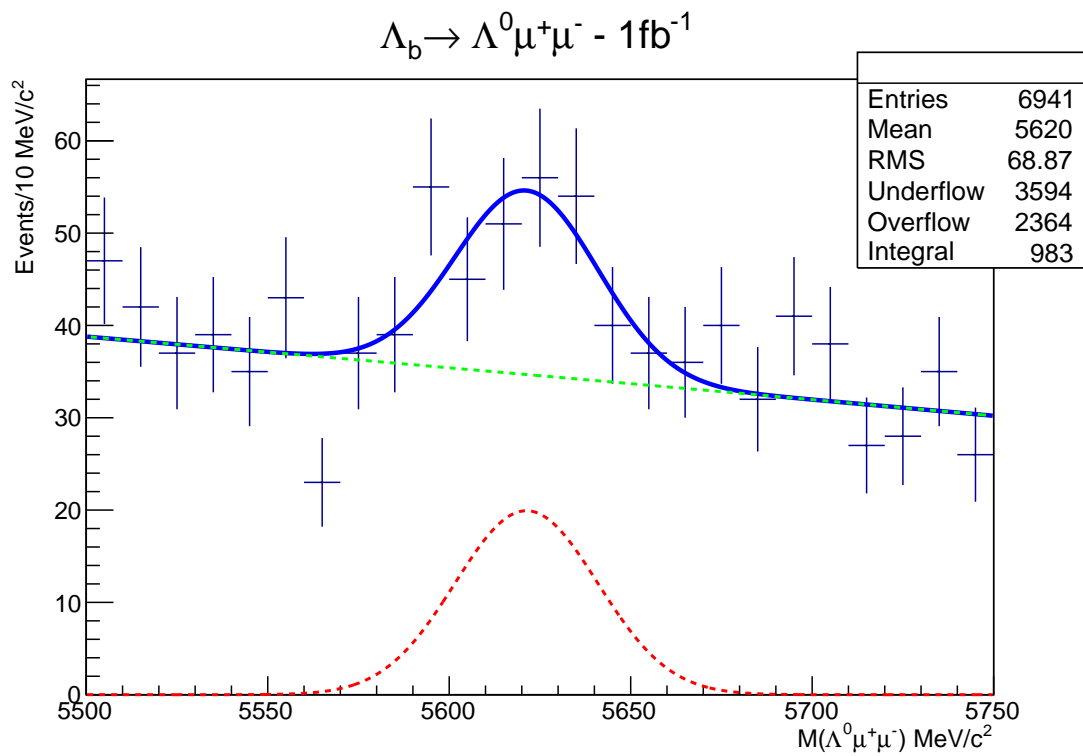
Chapter 5

Conclusion

The decay $\Lambda_b \to \Lambda \mu^+ \mu^-$ was observed with a $\frac{S}{\sqrt{S+B}} \approx 4.8\sigma$. The branching ratio of $\Lambda_b \to \Lambda \mu^+ \mu^-$ relative to the resonant decay $\Lambda_b \to \Lambda^0 J/\psi(1S)$ $(J/\Psi \to \mu^+ \mu^-)$ was measured to be $\mathcal{R} = 1.89 \times 10^{-3}$. The only previous measurement of this value was performed by the CDF experiment. The quoted figure is in agreement with our measurement with $\mathcal{R} = (2.45 \pm 0.59 \pm 0.29) \times 10^{-3}$ [17]. Sources of error in our measurement come from the methods used to calculate the relevant efficiencies. The largest contribution to those comes from the trigger efficiency where the TISTOS method was used. The biggest source of error comes from the fitting of the data. A more accurate result could have been obtained with a more thorough fitting procedure and multivariate approach to optimising the selection, but this is beyond the scope of these studies and will form the basis for future work within LHCb.

Appendix A

Hlt1TrackMuon Requirements			
Single Muon		Dimuon	
High P_T	Standard	Low Mass	High Mass
P $> 8000 MeV$	P $> 6000 MeV$	P $> 6000 MeV$	P $> 6000 MeV$
$P_T > 4800 MeV$ Track $\chi^2 < 4$ GEC = 'loose'	$P_T > 1300 MeV$ Track $\chi^2 < 4$ N Track Hits > 16 N VELO Hits > 9 GEC = 'loose'	$P_T > 500 MeV$ Track $\chi^2 < 4$ Vertex DOCA < 0.2 Vertex $\chi^2 < 25$ GEC = 'loose' Mass > 1000 IP $\chi^2 < 9$	$P_T > 500 MeV$ Track $\chi^2 < 4$ Vertex DOCA < 0.2 Vertex $\chi^2 < 25$ GEC = 'loose' Mass > 2900

Table A.1: Hlt1TrackMuon requirements. GEC - Global Event Cut. DOCA - Distance Of Closest Approach

Bibliography

[1] American Association for the Advancement of Science (AAAS) - www.aaas.org

[2] S.L. Glashow, *Nucl. Phys.* **22**, 4, 579-588 (1961).

[3] A. Salam, *Nobel Symposium 8, 'Elementary Particle Theory: Relativistic Groups and Analyticity*, 367-377 (1968)

[4] S. Weinberg, *Phys. Rev. Lett.* **19** 21, 1264-1266 (1967).

[5] J. Beringer *et al.* (Particle Data Group), *Phys. Rev. D* **86**, 010001 (2012).

[6] M.A. Thomson, "Lecture notes for the 2011 RAL School for Experimental High Energy Physics Students", RAL Technical Reports *RAL-TR-2011-014* (2011).

[7] CMS Collaboration, *arXiv:1207.7235v1* (2012).

[8] ATLAS Collaboration, *arXiv:1207.7214v1* (2012).

[9] M.J. Aslam, Yu-Ming Wang, Cai-Dian Lü *arXiv:0808.2113v1* (2008).

[10] The LHCb Collaboration, *JINST* **3 S08005** (2008).

[11] A. Ali, P. Ball, L. T. Handoko, G. Hiller, *Phys. Rev. D* **61**, 074024 (2000).

[12] Chaun-Hung Chen, C.Q. Geng, *Phys. Lett. B* **516**, 327-336 (2001).

[13] E. Lunghi, J. Matias, *JHEP* **04 058**, (2007).

[14] Chaun-Hung Chen, C.Q. Geng, *Phys. Rev. D* **63**, 114024 (2001).

[15] The LHCb Collaboration, *Phys. Lett. B* **694**, 209216 (2010).

[16] The LHCb Collaboration, *LHCb-PAPER-2011-018* (2011).

[17] CDF Collaboration, *arXiv:1107.3753v1* (2011).

[18] The LHCb Collaboration, *LHCb-CONF-2011-027* (2011).

[19] T. Sjöstrand, S. Mrenna, P. Skands, *hep-ph 0603175 LU TP 0613 FERMILAB-PUB-06-052-CD-T* (2006).

[20] A. Ryd, D. Lange, N. Kuznetsova, et al, *BAD 522 V6 EvtGen V00-11-06* (2004).

[21] B.P. Roea, Hai-Jun Yang,J. Zhu, Y. Liu, I. Stancu,G. McGregor, *NIMPR* **A 543**, 577-584 (2005).

[22] J.A. Hernando Morata *et al.*, "Measurement of trigger efficiencies and biases", *LHCb-2008-073*.